

Varstrometry for Off-nucleus and Dual sub-Kpc AGN (VODKA): Hubble Space Telescope Discovers Double Quasars

YU-CHING CHEN,^{1,2,3} HSIANG-CHIH HWANG,⁴ YUE SHEN,^{1,2} XIN LIU,^{1,2} NADIA L. ZAKAMSKA,⁴ QIAN YANG,¹ AND JENNIFER I. LI¹

¹*Department of Astronomy, University of Illinois at Urbana-Champaign, Urbana, IL 61801, USA*

²*National Center for Supercomputing Applications, University of Illinois at Urbana-Champaign, Urbana, IL 61801, USA*

³*Center for AstroPhysical Surveys, National Center for Supercomputing Applications, Urbana, IL, 61801, USA*

⁴*Department of Physics and Astronomy, Johns Hopkins University, Baltimore, MD 21210, USA*

ABSTRACT

Dual supermassive black holes (SMBHs) at \sim kpc scales are the progenitor population of SMBH mergers and play an important role in understanding the pairing and dynamical evolution of massive black holes in galaxy mergers. Because of the stringent resolution requirement and the apparent rareness of these small-separation pairs, there are scarce observational constraints on this population, with few confirmed dual SMBHs at < 10 kpc separations at $z > 1$. Here we present results from a pilot search for kpc-scale dual quasars selected with *Gaia* Data release 2 (DR2) astrometry and followed up with *Hubble Space Telescope* (*HST*) Wide Field Camera 3 dual-band (F475W and F814W) snapshot imaging. Our targets are quasars primarily selected with the varstrometry technique, i.e., light centroid jitter caused by asynchronous variability from both members in an unresolved quasar pair, supplemented by sub-arcsec pairs already resolved by *Gaia* DR2. We find an overall high fraction of *HST*-resolved pairs among the varstrometry-selected quasars (unresolved in *Gaia* DR2), $\sim 30 - 50\%$, increasing toward high redshift ($\sim 60 - 80\%$ at $z > 1.5$). We discuss the nature of the 45 resolved sub-arcsec pairs based on *HST* and supplementary data. A substantial fraction ($\sim 40\%$) of these pairs are likely physical quasar pairs or gravitationally lensed quasars. We also discover a triple quasar candidate and a quadruply lensed quasar, which is among the smallest-separation quadruple lenses. These results provide important guidelines to improve varstrometry selection and follow-up confirmation of \sim kpc-scale dual SMBHs at high redshift.

Keywords: black hole physics — galaxies: active — quasars: general — surveys

1. INTRODUCTION

Since most massive galaxies harbor a central supermassive black hole (SMBH; Kormendy & Richstone 1995; Kormendy & Ho 2013), galaxy mergers should result in the formation of dual SMBHs and eventually binary SMBHs (Begelman et al. 1980). Dual SMBHs are the precursors of binary SMBHs. A binary SMBH is on a compact ($\lesssim 10$ parsec) orbit in its own potential whereas a dual SMBH is on wider orbits and evolving in the potential of the (merged) host galaxy. Theory predicts strong gravitational waves (GWs) from the final coalescence of merging SMBHs – a “standard siren” for cosmology and a direct testbed for strong-field general relativity (Hughes 2009; Centrella et al. 2010). The presence of gas accretion during the merger process can dramatically change the expectations for the duration of the gravitational-wave-emitting phase (Bogdanovic et al. 2021).

Before the binary SMBH stage, the two black holes spend several hundred million years in the dual SMBH stage as the galaxy merger proceeds. The observational search of close (\sim kpc) dual quasars at $1 < z < 3$ is particularly important for constraining the merger process, because the effects of mergers are believed to be the most significant in the high-redshift, high-luminosity, and close-separation regime (Hopkins et al. 2008). The redshift range $1 < z < 3$ is also where we expect the horizon of the stochastic gravitational wave background from the ensemble of SMBH binaries (Arzoumanian et al. 2018).

In the past decade, significant progress has been made toward finding concrete evidence for active merging SMBHs in kpc-scale dual active galactic nuclei (AGN) (De Rosa et al. 2020). The majority of known dual AGN are at low redshifts and/or at large physical separations (> 20 kpc, Figure 1), and many have relatively low luminosities. Little is known about dual SMBHs at

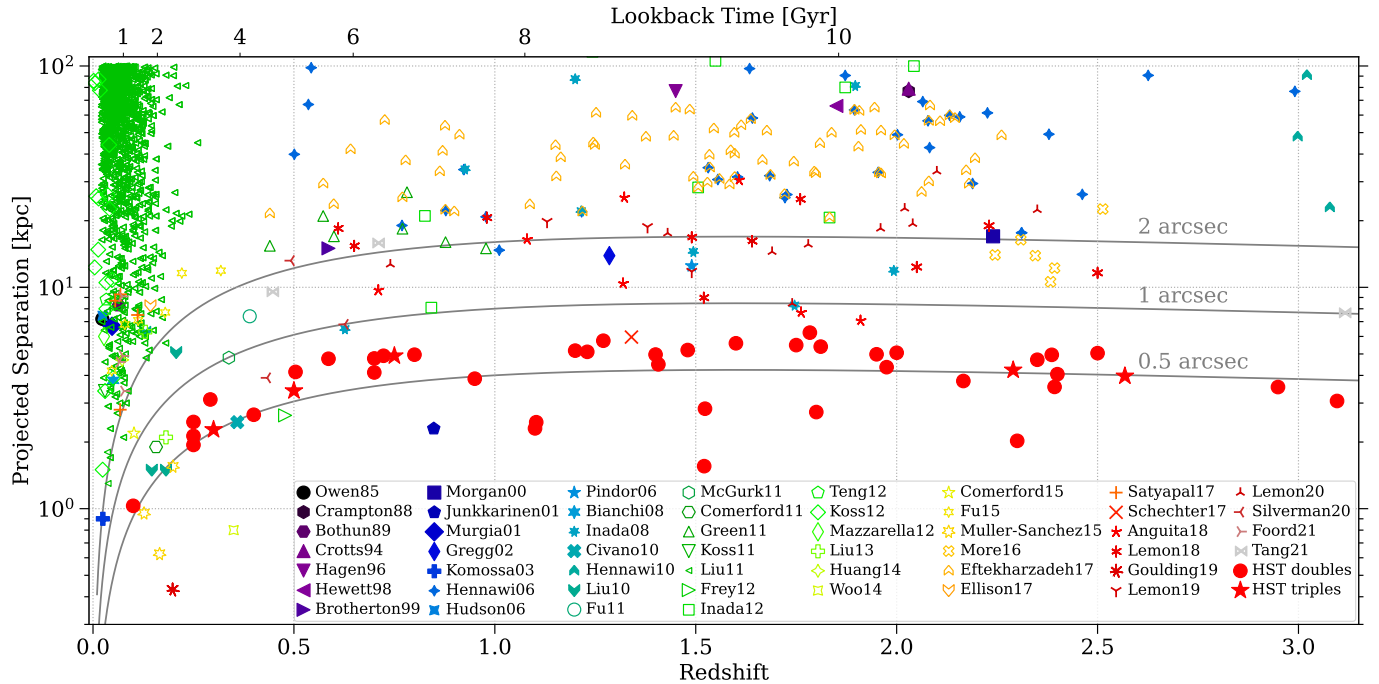


Figure 1. Quasars with double/triple sources discovered by *HST*/WFC3 imaging in comparison to their reported dual quasars in the literature (Owen et al. 1985; Crampton et al. 1988; Bothun et al. 1989; Crotts et al. 1994; Hagen et al. 1996; Hewett et al. 1998; Brotherton et al. 1999; Morgan et al. 2000; Junkkarinen et al. 2001; Murgia et al. 2001; Gregg et al. 2002; Komossa et al. 2003; Hennawi et al. 2006; Hudson et al. 2006; Pindor et al. 2006; Bianchi et al. 2008; Inada et al. 2008; Civano et al. 2010; Hennawi et al. 2010; Liu et al. 2010a; Fu et al. 2011; McGurk et al. 2011; Comerford et al. 2011; Green et al. 2011; Koss et al. 2011; Liu et al. 2011; Frey et al. 2012; Inada et al. 2012; Teng et al. 2012; Koss et al. 2012; Mazzarella et al. 2012; Liu et al. 2013; Huang et al. 2014; Woo et al. 2014; Comerford et al. 2015; Fu et al. 2015a; Müller-Sánchez et al. 2015; More et al. 2016; Eftekharzadeh et al. 2017; Ellison et al. 2017; Satyapal et al. 2017; Schechter et al. 2017; Anguita et al. 2018; Lemon et al. 2018; Goulding et al. 2019; Lemon et al. 2019, 2020; Silverman et al. 2020; Foord et al. 2021; Tang et al. 2021). A dual quasar is defined as a quasar pair with velocity differences $< 2000 \text{ km s}^{-1}$. Shown here is the projected physical separation as a function of redshift. No confirmed dual quasar is known at $r_p < 6 \text{ kpc}$ at $z > 1$. Our sample probes this new parameter space.

the cosmic “high noon” (i.e., $1 < z < 3$), when both the number density of luminous quasars and the global star formation rate density peak (Richards et al. 2006; Madau & Dickinson 2014). Finding small-separation dual quasars at high redshifts is extremely difficult observationally due to the typical sizes of the point-spread functions (PSFs) of ground-based optical surveys. There is only one 2.3 kpc dual quasar known at $z \sim 0.8$ from a serendipitous discovery (Junkkarinen et al. 2001; Shields et al. 2012) and five dual quasars with $6 < r_p < 10 \text{ kpc}$ at $0.5 < z \lesssim 3$ from systematic searches (Inada et al. 2012; More et al. 2016; Lemon et al. 2018; Silverman et al. 2020; Tang et al. 2021, see Figure 1 for details). From a theoretical perspective, the dynamical evolution of dual SMBHs in merged galaxies can be well described by dynamical friction before entering the GW-dominated regime (Yu 2002; Merritt 2013; Chen et al. 2020a), which results in shorter time spans on smaller separations. Therefore, the frequency of $\lesssim \text{kpc}$ dual SMBHs is expected to be substantially lower than those on $\sim \text{tens of kpc}$ separations, requiring an effi-

cient targeting scheme to identify candidates for follow-up confirmation.

Although not the focus of this work, searches for binary SMBHs ($\lesssim 10 \text{ parsec}$) are even more challenging. There are only two reported cases of (candidate) binary SMBHs resolved with the Very Long Baseline Array (VLBA) imaging at 7 parsec (Rodríguez et al. 2006) and 0.35 parsec (Kharb et al. 2017) from serendipitous searches. While searches using indirect methods (from periodic light curves or radial velocity shifts of broad emission lines, Eracleous et al. 2012; Shen et al. 2013; Liu et al. 2014; Graham et al. 2015; Charisi et al. 2016; Runnoe et al. 2017; Wang et al. 2017; Guo et al. 2019; Liu et al. 2019; Chen et al. 2020b; Liao et al. 2021) have yielded candidates of sub-pc binary SMBHs, alternative scenarios involving single SMBHs remain possible. Direct imaging confirmation for most of these sub-pc binary candidates is not feasible even with Very Long Baseline Interferometry (VLBI) in radio due to strict angular resolution requirement (Burke-Spolaor 2011).

Shen et al. (2019) and Hwang et al. (2020) have proposed a new astrometric technique, **varstrometry**, with *Gaia* data (Gaia Collaboration et al. 2018) to discover close (sub-arcsecond) dual/lensed quasars (also see Williams & Saha 1995; Liu 2015; Springer & Ofek 2021). It takes advantage of the ubiquitous quasar variability, which in dual or lensed quasars results in an astrometric noise signature when the asynchronous variability from the two quasars causes centroid jitters in the unresolved system. *Gaia*’s full-sky coverage and depth to $G \sim 21$ mag (reaching $\sim 7 \times 10^5$ extragalactic objects) enable a large-scale systematic search in the poorly explored sub-arcsecond regime at high redshift (Hwang et al. 2020; Shen et al. 2021).

In this work, we report the first results from a pilot *HST* dual-band imaging program to follow up the *Gaia*-astrometry-selected dual/lensed quasar candidates. It reveals compact double or triple sources in the 45 targets, 40% of which are possible dual/lensed quasars based on the *HST* two-band colors. The targets that are not quasar-star superpositions are more likely to be dual quasars instead of lenses, which require very massive lenses at high redshifts given the non-detection of the lens galaxy in the *HST* image (Shen et al. 2021).

The paper is organized as follows. In §2, we describe the methodology and the data we use for this study. We present our main results in §3 and discuss their implications and future prospects in §4. We summarize our findings in §5. Throughout this paper we focus on optically unobscured, broad-line quasars, for which we can apply this **varstrometry** technique, and all physical separations are the projected separation. A flat Λ CDM cosmology is adopted throughout with $\Omega_\Lambda = 0.7$, $\Omega_m = 0.3$, and $H_0 = 70 \text{ km s}^{-1} \text{ Mpc}^{-1}$.

2. OBSERVATIONS AND DATA ANALYSIS

2.1. Target Selection

Our parent quasar sample includes both spectroscopically confirmed SDSS DR7 quasars (Shen et al. 2011b) and DR14 quasars (Pâris et al. 2018), and photometrically selected quasar candidates based on WISE (Wright et al. 2010; Mateos et al. 2012; Secrest et al. 2015). The target selection criteria are mainly based on *Gaia* DR2 (Gaia Collaboration et al. 2018). Our targets are selected as *Gaia*-unresolved quasars with excess astrometric noise (i.e., **varstrometry** selection) and quasars with a sub-arcsec companion resolved in *Gaia* data (Hwang et al. 2020). For *Gaia*-unresolved sources, we use **astrometric_excess_noise** (Lindgren et al. 2012, 2018) as a surrogate for the astrometric jitters caused by **varstrometry** (Hwang et al. 2020; Shen et al. 2019). For *Gaia*-resolved sources, we prioritize pairs with small

angular separations ($0''.4$ – $0''.7$) and use other information (see below) to reduce chance superposition stars. The *Gaia*-resolved sources are intended to increase the statistics on sub-arcsec pairs in quasars, since *HST* is able to resolve these pairs and derive color/morphology information, though they are at wider separation due to the minimal separation limit of $0''.4$ in *Gaia* DR2 (Arenou et al. 2018).

The detailed target selection and target categories are:

1. SDSS quasars with a single *Gaia* match within $3''$ (40 targets selected). We use both the SDSS DR7 quasar catalog (Shen et al. 2011b) and the DR14 quasar catalog (Pâris et al. 2018). Because the extended structure of low-redshift host galaxies may also result in a high **astrometric_excess_noise** (Hwang et al. 2020), we apply a redshift cut of $z > 0.5$ and require that the source is flagged as non-extended in all filters of Pan-STARRS1 (Chambers et al. 2016). To reduce contamination from foreground stars, we exclude sources where the SDSS fiber ($2''$ or $3''$) spectra have obvious stellar features. Then, we select 8 targets that have **astrometric_excess_noise** > 3.39 mas and *Gaia* *G*-band magnitude < 19.5 mag, and additional 32 targets that have **astrometric_excess_noise** > 1.44 mas and *Gaia* *G*-band magnitude < 19.1 mag. These magnitude cuts restrict the selection to reliable *Gaia* astrometry.
2. WISE+Pan-STARRS1 quasars with a single *Gaia* match within $3''$ (40 targets selected). We use an all-sky photometric quasar sample selected with WISE data (Mateos et al. 2012; Secrest et al. 2015) and the cross-match catalog provided by *Gaia* DR2 (Marrese et al. 2019). We further require that the target is flagged as non-extended in all filters in Pan-STARRS1 (Chambers et al. 2016). To reduce contamination from stars misclassified as quasars in the photometric quasar catalog, we exclude targets that have non-zero total proper motions at $> 3\sigma$. Then, we select 40 targets that have the largest **astrometric_excess_noise** (> 1.52 mas) with *Gaia* *G*-band magnitude < 19.15 mag.
3. WISE-only quasars without SDSS and Pan-STARRS1 information and with a single *Gaia* match within $3''$ (20 targets selected). We select WISE quasars (Mateos et al. 2012; Secrest et al. 2015; Marrese et al. 2019) that are not covered by Pan-STARRS1 (Chambers et al. 2016). Without the optical imaging information, this sample has a higher risk of being affected by extended host galaxies at low redshifts. Specifically, we find

that if we select the WISE quasars with highest `astrometric_excess_noise` directly, our sample is dominated by low-redshift, extended galaxies upon inspecting their optical images from the DECam Legacy Survey (DECaLS, Dey et al. 2019).

To improve the selection, we impose an additional criterion on `phot_bp_rp_excess_factor`, which is a quality indicator for *Gaia* photometry (Riello et al. 2018). In *Gaia* DR2, G-band photometry is measured by PSF fitting, while the BP and RP photometry is the sum of fluxes in a $3''.5 \times 2''.1$ window (no de-blending treatment, Riello et al. 2018). Therefore, the ratio between the G-band flux and the sum of BP- and RP-fluxes (`phot_bp_rp_excess_factor`) can be used as a measure of how PSF-like a target is. Specifically, here we select WISE-only quasars with `phot_bp_rp_excess_factor` < 1.5. Then we select the targets with `astrometric_excess_noise` between 1.5 and 2.5 mas, *Gaia* proper motions consistent with 0 within 3σ , and *Gaia* G-band magnitude < 19.3 mag. We avoid `astrometric_excess_noise` > 2.5 mas because the images from DECaLS (if available) suggest that many of them may still be affected by extended host galaxies. A color cut of BP-RP < 2.5 is also imposed because we find it particularly useful to avoid low-redshift ($z < 0.5$) galaxies. Despite precautions, this WISE-only sample may have a high rate of contamination by stars and/or by low-redshift host galaxies. We thus prioritize the targets with larger `astrometric_excess_noise` and limit the number of the proposed *HST* targets to 20.

4. SDSS quasars with multiple *Gaia* matches (20 targets selected). The selection is similar to the single-matched SDSS quasars, but here the targets have multiple *Gaia* matches within $3''$. To reduce chance projection of foreground stars, we exclude sources that have non-zero parallaxes or non-zero proper motions with significance > 3σ , and exclude those having obvious stellar features in the SDSS spectra. Two targets have three *Gaia* matches (J121135.93+354417.6 and J133039.82−001035.7), and the other targets have two *Gaia* matches. We prioritize targets with small angular separations ($0''.52$ – $0''.73$), which are usually unresolved by ground-based surveys. Since this selection does not involve `astrometric_excess_noise`, we do not impose

Table 1. Summary of *HST* sample statistics. Listed are the number of dual/lensed quasar candidates selected using *Gaia* DR2, the number of candidates observed by *HST*, and the number of candidates containing multiple sources.

Target Category	# targeted	# observed	# multiple
1. SDSS Single	40	17	9
2. WISE+PS1 Single	40	26	7
3. WISE-only Single	20	13	2
4. SDSS Multiple	20	7	7
5. WISE+PS1 Multiple	20	15	15
6. WISE-only Multiple	10	6	5
Total	150	84	45

any cuts on spectroscopic redshift and G-band magnitude.

5. WISE+Pan-STARRS1 quasars with multiple *Gaia* matches (20 targets selected). The selection is similar to the single-matched WISE+Pan-STARRS1 quasars, but here the targets have multiple *Gaia* matches within $3''$. We exclude sources that have non-zero parallaxes or proper motions with significance > 3σ . We prioritize targets with small angular separations ($0''.48$ – $0''.66$).
6. WISE-only quasars with multiple *Gaia* matches (10 targets selected). We exclude sources that have non-zero parallaxes or proper motions with significance > 3σ , and we prioritize targets with small angular separations ($0''.46$ – $0''.60$).

Our final target sample for the *HST* follow-up observations consists of 150 quasars. Table 1 summarizes the numbers of the proposed targets, the observed targets and the pairs discovered by the *HST* in each category. The top panel of Figure 2 shows the distributions of redshift and SDSS *r*-band PSF magnitude for the 60 targets selected from SDSS. The bottom panel of Figure 2 shows the distributions of *Gaia* `astrometric_excess_noise` and G-band magnitude for the final target sample.

2.2. *HST*/WFC3 F475W and F814W Imaging

We observed 84 out of the 150 targets with the Wide Field Camera 3 (WFC3) on board the *HST* in Cycle 27 and 28 from 2019 October 9 UT to 2021 September 23 UT (Program ID: SNAP-15900; PI: Hwang). Each target was imaged in the UVIS/F475W (with pivot wavelength $\lambda_p = 4773\text{\AA}$ and effective width of 1344\AA) and UVIS/F814W (with $\lambda_p = 8024\text{\AA}$ and effective width of 1536\AA) filters within a single *HST* SNAP orbit to help distinguish stars and quasars. The typical net exposure times are 360s in the F475W filter and 400s in the F814W filter for each target and are scaled for fainter

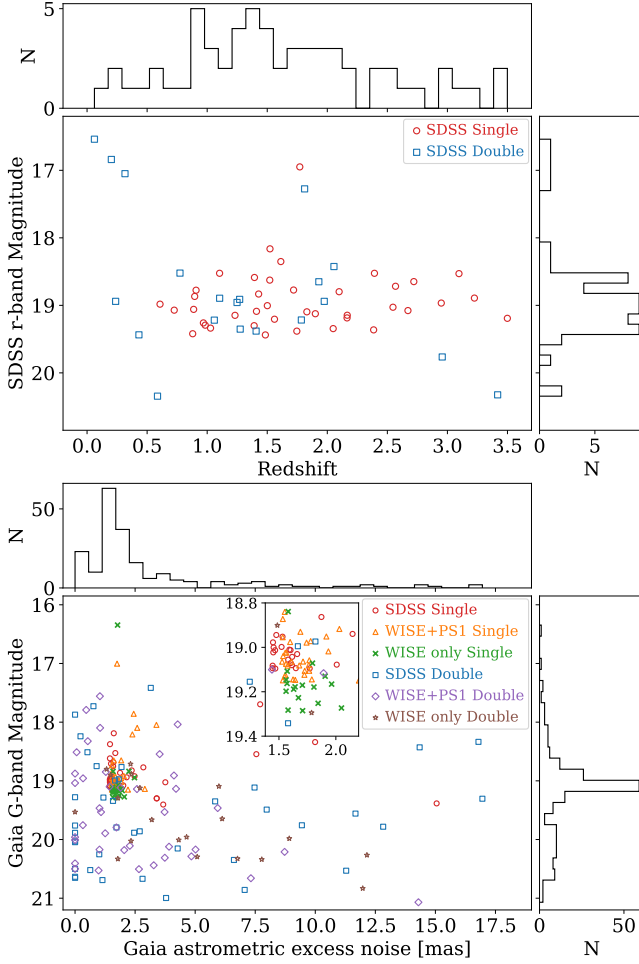


Figure 2. *Top:* Distribution of redshift and SDSS r-band PSF magnitude for the 60 targets selected from SDSS. *Bottom:* Distribution of the *Gaia* `astrometric_excess_noise` and G-band magnitude for the final target sample of 150.

targets to reach similar signal-to-noise ratios. Table 2 lists the spectroscopic and photometric properties and the observation details for all the observed targets. Target names are in the form of “hhmmss.ss±ddmmss.s” based on *Gaia* DR2; the coordinates of the brightest source are used if multiple sources are detected in *Gaia*. Magnitudes are reported in ST magnitude ($m_{ST} = -2.5\log(F_\lambda) - 21.1$), where F_λ is in units of $\text{erg s}^{-1} \text{cm}^{-2} \text{\AA}^{-1}$.

The F475W filter covers rest-frame 1600–2200 Å and the F814W filter covers rest-frame 2800–3800 Å at the median redshift $z \sim 1.5$ of our targets. They sample the ultraviolet part of the quasar spectrum. We use these two bands to derive the F475W–F814W color to facilitate the interpretation of resolved pairs.

The WFC3-UVIS charge-coupled device (CCD) has a sampling of $0''.04 \text{ pixel}^{-1}$. The observations were dithered at 4 positions to properly sample the PSF and

to reject cosmic rays and bad pixels. A 512×512 sub-array was employed, yielding a field of view (FOV) of $20.5'' \times 20.5''$.

We reduced the *HST* images following standard procedures. We used the `calwf3` and `MultiDrizzle` tasks from the STSDAS package in PyRAF. We processed the images with `MultiDrizzle` to correct for geometric distortion and pixel area effects. We combined the dithered frames and rejected cosmic rays and hot pixels. The resulting images are photometrically and astrometrically calibrated. `MultiDrizzle` relies on the positions of guide stars for absolute astrometric calibration. The absolute astrometric accuracy of the reduced images is limited by the positional uncertainty of guide stars ($\gtrsim 0''.2$) and the calibration uncertainty of the fine guidance sensor to the instrument aperture ($\sim 0''.015$). The image relative astrometric accuracy is limited by the uncertainty in the geometric distortion correction of the camera. The typical relative astrometric accuracy is $0''.004$.

2.3. Surface Brightness Decomposition

We perform 2-dimensional (2-D) surface brightness decomposition with GALFIT (Peng et al. 2010). GALFIT fits the image with 2-D functions including PSF, Sérsic profiles and various structures such as rings and spiral arms for galaxies and point sources.

The PSF model is constructed using a nearby isolated star in the same field for each target. For those targets without nearby field stars or when the field stars are too faint, we use a general model made from a bright isolated star in one of the visits.

Since our SNAP observations are generally too shallow to detect faint features, a PSF model is often sufficient to fit each component of the resolved pair. A Sérsic component with Sérsic index $n = 4$ is added in the fit if the residuals show significant extended features.

2.4. Photometric Redshift

For the 60 observed targets without a spectroscopic redshift, we estimate photometric redshifts (photo- z s) with Skewt-QSO¹. Skewt-QSO can achieve a photo- z accuracy, defined as the fraction of quasars with the difference between the photo- z and the spectroscopic redshift within 0.1, of 72%–79% using optical photometry from Pan-STARRS1 or DECaLS with *WISE* W1 and W2 data (Yang et al. 2017). We use optical photometric data from Pan-STARRS1, or *Gaia* if Pan-STARRS1 is not available, in combination with *WISE* W1 and W2 mid-infrared photometry. The photo- z s are labeled with dagger symbols in Table 2 and Table 3.

¹ <https://github.com/qian-yang/Skewt-QSO>

Table 2. Target properties and log of the *HST* observations.

Name	Redshift	r	G	Ast. excess noise	Std.(Flux)	Obs. date	Exp. time	Cat.
		[mag]	[mag]	[mas]	[e ⁻ s ⁻¹]	[UT]	[s]	
(1)	(2)	(3)	(4)	(5)	(6)	(7)	(8)	(9)
J000514.20+702249.2*	0.7 [†]	...	18.54/18.85	3.522/1.283	72.1/21.6	2020-01-24	360/320	5
J004127.74−734706.4	1.3 [†]	...	16.35	1.771	225.1	2019-11-14	40/40	3
J014859.18−553037.5*	0.1 [†]	...	18.71/18.90	2.309/1.486	33.7/46.7	2020-08-24	320/320	6
J023959.20−190507.5	0.75 [†]	...	19.11	1.766	35.1	2020-07-15	360/600	2
J024134.91+780107.0*	2.35 [†]	...	18.95	1.917	23.6	2020-01-31	400/320	2
J024205.24−453805.2	1.3 [†]	...	19.16	1.571	40.5	2020-08-28	360/400	3
J024628.63+692234.0*	0.95 [†]	...	18.04/19.12	4.272/1.892	12.6/16.0	2019-10-13	1080/80	5
J024804.31−281449.9	1.9 [†]	...	18.98	1.598	34.4	2019-10-20	320/400	2
J024929.19−002104.3	1.428	18.84	18.71	1.497	48.4	2019-10-19	360/320	1
J025359.01−282653.6	2.0 [†]	...	19.02	1.566	48.0	2021-08-25	520/440	2
J025843.71+690543.4	0.1 [†]	...	18.92	2.031	37.9	2019-10-12	1320/240	2
J025956.93−735316.8	0.85 [†]	...	19.11	1.573	39.8	2019-11-09	360/480	3
J032233.97−551532.9	0.1 [†]	...	18.80/19.09 ^a	1.314/5.986 ^a	98.3/24.6 ^a	2020-10-04	320/320	6
J034828.66−401513.1*	2.4 [†]	...	19.29	1.708	42.0	2020-09-30	400/440	3
J045528.99−445637.6*	0.5 [†]	...	19.98/20.83	8.917/11.975	27.7/15.0	2020-08-09	360/400	6
J045905.23−071407.1*	0.25 [†]	...	21.07/20.21	14.294/8.723	13.5/23.0	2020-02-05	360/400	5
J053620.23+503826.2*	1.8 [†]	...	17.86	2.442	94.2	2020-08-07	320/320	2
J054721.54−321309.5	0.3 [†]	...	19.04	1.537	50.0	2019-11-05	360/320	2
J055321.99+374004.5	0.35 [†]	...	19.12	1.556	68.5	2019-12-14	480/400	2
J055455.69+511252.8*	0.7 [†]	...	18.51/20.50	0.066/2.661	51.8/12.8	2020-02-23	320/320	5
J060155.15−071007.3	1.95 [†]	...	19.08	1.576	33.4	2019-12-09	480/400	2
J060734.57−064838.5*	2.3 [†]	...	18.10	2.587	91.1	2020-04-23	1320/80	2
J062026.53−071144.2	0.75 [†]	...	19.02	1.935	33.0	2020-01-30	360/400	2
J062903.08−753642.8*	0.3 [†]	...	19.65/20.02	6.126/2.329	72.0/25.6	2020-05-09	360/400	6
J074800.55+314647.4*	1.407	19.32	20.25/20.05	0.0/1.008	27.3/17.9	2020-04-18	360/400	4
J074817.13+191003.0*	3.096	18.49	18.94	2.147	78.8	2021-05-06	320/320	1
J074922.96+225511.7*	2.166	19.11	18.62	1.452	95.4	2020-01-05	320/400	1
J074930.93+505859.7	0.907	18.77	19.06	1.581	24.7	2019-12-01	360/480	1
J075350.57+424743.9*	1.523	18.14	18.19	1.613	64.5	2020-02-05	320/320	1
J075824.26+145752.4*	2.568	18.75	19.30	3.400	46.7	2020-09-28	360/400	1
J080414.01−443515.4	1.85 [†]	...	19.20	1.562	25.1	2020-07-31	360/400	3
J081603.79+430521.1*	0.586	20.08	20.86/20.67	7.062/2.810	32.5/20.2	2019-12-08	360/400	4
J082341.08+241805.6*	1.811	17.17	18.24/17.87	0.227/0.0	84.1/120.5	2020-01-16	320/320	4
J084129.77+482548.4*	2.949	18.87	19.30	3.399	37.4	2019-11-30	360/400	1
J090408.66+333205.2*	1.103	18.50	18.55	7.546	93.7	2020-01-24	320/320	1
J090501.12+585902.5*	2.386	19.33	18.53	1.676	63.6	2020-04-29	320/320	1
J091826.08+351243.1*	1.521	18.64	18.77	2.845	45.7	2021-01-13	360/320	1

Table 2 continued

Table 2 (*continued*)

Name	Redshift	r	G	Ast. excess noise	Std.(Flux)	Obs. date	Exp. time	Cat.
		[mag]	[mag]	[mas]	[e ⁻ s ⁻¹]	[UT]	[s]	
(1)	(2)	(3)	(4)	(5)	(6)	(7)	(8)	(9)
J091938.93+621951.1*	1.270	18.81	20.52/18.75	0.633/0.898	12.8/34.5	2020-12-13	320/320	4
J094007.41+334609.5*	1.784	19.04	19.49/19.76	7.978/9.445	89.8/17.3	2020-01-07	360/400	4
J095611.62+425459.7	0.968	19.26	19.01	1.602	78.5	2019-10-09	520/600	1
J102531.00+414024.0	1.746	19.37	19.08	2.008	32.2	2020-06-16	360/400	1
J105929.04−503739.5*	0.25 [†]	...	18.84	2.243	32.5	2021-08-25	320/320	3
J111841.61+220015.9	1.394	18.59	18.98	1.448	38.3	2019-11-02	320/400	1
J113302.56+475623.0	0.984	19.29	18.95	1.531	33.8	2020-01-25	360/400	1
J122734.48−491202.5*	0.25 [†]	...	20.30/20.01	5.086/4.316	28.5/37.8	2020-07-21	360/400	6
J131416.01−491218.2*	2.29	...	19.29/19.53	1.787/0.0	27.617.6	2019-12-26	400/440	6
J132614.08+063909.9	2.165	19.19	19.07	1.604	23.2	2020-01-05	360/400	1
J133040.00−125135.7	2.4 [†]	...	19.06	1.609	46.2	2019-12-18	360/480	2
J133952.42−074828.6	0.6 [†]	...	19.07	1.562	30.7	2020-02-24	360/400	2
J135531.37−084212.1	1.05 [†]	18.02	18.84	1.551	35.5	2020-04-10	320/320	2
J140518.25−050607.7	1.2 [†]	...	19.11	1.727	50.8	2020-02-04	520/600	2
J142346.38−233844.7	0.15 [†]	...	18.98	1.745	31.0	2021-04-27	360/320	2
J151041.67+022134.3	1.232	19.15	18.94	1.477	28.3	2020-05-19	320/400	1
J155542.38−082826.9	0.3 [†]	...	19.02	1.556	30.7	2020-08-25	360/320	2
J161349.51−264432.5*	1.1 [†]	...	19.15	2.203	84.7	2020-01-31	480/400	2
J162319.31−044703.2	1.55 [†]	...	18.95	1.533	50.8	2020-06-08	360/400	2
J164818.07+415550.1*	2.393	18.50	18.38	1.456	50.3	2021-06-03	320/320	1
J164941.29+081233.5*	1.4 [†]	...	18.32/19.46	0.530/1.020	76.2/17.4	2020-09-10	320/320	5
J171139.97−161147.9*	0.75 [†]	...	20.29/19.46	4.842/5.938	14.9/46.5	2020-05-06	360/400	5
J173222.88−133535.2*	0.292	...	19.08	1.762	49.1	2019-10-22	520/400	2
J175543.18+422924.2*	1.95 [†]	17.66	20.44/17.79	3.275/0.464	16.2/80.9	2020-02-17	320/320	5
J180409.55+323029.5*	0.504	...	19.14/19.76	4.203/0.327	63.8/17.6	2020-01-06	360/320	5
J183353.81−475524.9	0.65 [†]	...	19.23	1.671	30.0	2020-03-24	400/440	3
J184520.85−232227.6*	0.8 [†]	...	19.03/19.53	0.0/1.081	30.9/15.3	2021-09-23	320/320	5
J185226.10+483315.0*	1.480	...	19.14	2.906	30.9	2020-02-06	360/400	2
J185728.65+704811.3*	1.230	...	19.53/20.53	3.727/0.980	23.4/14.9	2019-10-20	360/400	5
J192843.97+643244.1	0.35 [†]	...	19.14	1.789	36.2	2019-11-02	520/400	2
J193547.95−554946.4	1.55 [†]	...	19.15	1.563	21.0	2020-03-17	360/400	3
J193711.89−163254.6	0.25 [†]	...	18.97	1.779	32.8	2020-03-15	360/400	2
J193718.81−182132.2*	1.2 [†]	...	20.31/20.11	3.736/2.279	14.0/15.5	2020-07-02	360/400	5
J194200.49−514724.2	0.65 [†]	...	19.18	1.807	51.7	2020-03-14	360/480	3
J194349.74−023819.1*	1.6 [†]	...	18.96/20.17	0.333/1.018	24.4/18.1	2020-06-27	320/320	5
J194859.87−341200.2	0.3 [†]	...	19.15	1.643	50.3	2020-03-18	360/240	2
J204848.00+625858.3*	2.5 [†]	...	20.41/20.18	0.0/2.047	17.8/16.5	2019-10-27	360/400	5
J205000.01−294721.7*	1.75 [†]	...	20.12/18.91	3.913/4.117	17.6/51.0	2020-03-21	360/320	5
J212243.01−002653.8 *	1.975	18.71	19.89/19.34	0.0/1.580	15.0/40.6	2019-12-04	360/400	4

Table 2 *continued*

Table 2 (*continued*)

Name	Redshift	r	G	Ast. excess noise	Std.(Flux)	Obs. date	Exp. time	Cat.
		[mag]	[mag]	[mas]	[e ⁻ s ⁻¹]	[UT]	[s]	
(1)	(2)	(3)	(4)	(5)	(6)	(7)	(8)	(9)
J215444.04+285635.3*	0.723	19.62	20.35/19.35	6.615/5.831	17.4/56.1	2019-12-02	360/400	4
J215732.70−510730.4	1.15 [†]	...	19.25	1.844	24.0	2020-05-10	400/440	3
J221849.86−332243.6*	0.35 [†]	...	20.66/20.17	7.320/5.016	19.8/27.6	2020-08-21	360/400	5
J230223.02−423647.8	1.0 [†]	...	19.13	1.906	26.9	2020-08-22	400/400	3
J232157.47−113055.2	0.75 [†]	...	19.12	1.724	29.2	2020-08-24	360/480	2
J232412.70+791752.3*	0.4 [†]	...	17.00	1.749	103.3	2020-01-30	320/320	2
J233643.38−480152.3	0.8 [†]	...	19.18	1.642	57.5	2020-08-28	360/400	3
J235128.30−503418.5	0.6 [†]	...	19.28	1.580	29.5	2020-07-31	400/440	3

NOTE—Col. 1: Coordinate names in the form of “hhmmss.ss±ddmmss.s” based on *Gaia* DR2; the coordinates of the brightest source are used when multiple sources are detected in *Gaia*. Targets with multiple sources in *HST* are marked with a star. Col. 2: Spectroscopic redshift or photometric redshift when denoted with “[†]”. Col. 3: SDSS r -band PSF magnitude. Col. 4: *Gaia* G -band mean magnitude. Col. 5: *Gaia* `astrometric_excess_noise`. Col. 6: Standard deviation of *Gaia* G -band flux ($=\text{phot_g_mean_flux_error} \times (\text{phot_g_n_obs})^{\frac{1}{2}}$). Col. 7: *HST* Observation date. Col. 8: *HST* Exposure time in F475W and F814W filters, respectively. Col. 9: Target category (see Table 1).

^aThough *Gaia* DR2 detects two sources in J0322−5515, the *HST* observations only reveal one source. Recent *Gaia* EDR3 (Gaia Collaboration et al. 2021) only shows one source in J0322−5515, which suggests that the second source in *Gaia* DR2 is an artifact.

Table 3. Properties of the 45 *HST* targets with multiple cores.

Name	Redshift	$\Delta\theta$	r_p	P.A.	F475W	F814W	Cat.	Classification
		[arcsec]	[kpc]	[deg]	[mag]	[mag]		
(1)	(2)	(3)	(4)	(5)	(6)	(7)	(8)	(9)
J000514.20+702249.2	0.7 [†]	0.58	4.1	279.8	19.81/20.08	19.02/19.08	5	dual/lensed quasar
J014859.18−553037.5	0.1 [†]	0.56	1.0	181.6	18.51/20.16	19.82/18.88	6	quasar+star
J024134.91+780107.0	2.35 [†]	0.58	4.7	126.8	19.44/23.19	19.56/21.36	2	quasar+star
J024628.63+692234.0	0.95 [†]	0.49	3.9	49.2	20.90/22.59	17.93/18.89	5	quasar+star
J034828.66−401513.1	2.4 [†]	0.50	4.1	186.7	19.26/21.07	20.20/21.96	3	dual/lensed quasar
J045528.99−445637.6	0.5 [†]	0.56	3.4	93.1	20.99/21.10/22.87	21.99/22.44/24.00	6	triple quasar ^d
J045905.23−071407.1	0.25 [†]	0.63	2.5	154.6	21.21/21.98	22.34/22.39	5	dual quasar ^d
J053620.23+503826.2	1.8 [†]	0.32	2.7	162.3	18.68/20.01	18.52/19.90	2	dual/lensed quasar
J055455.69+511252.8	0.7 [†]	0.67	4.8	77.4	18.56/21.36	19.33/20.94	5	quasar+star
J060734.57−064838.5	2.3 [†]	0.25	2.0	196.3	21.29/23.87	18.11/19.69	2	quasar+star
J062903.08−753642.8	0.3 [†]	0.51	2.3	61.1	19.96/22.04/24.10	21.12/20.61/22.28	6	quasar+stars
J074800.55+314647.4	1.407	0.53	4.5	171.1	20.13/20.54	21.04/20.58	4	dual/lensed quasar
J074817.13+191003.0	3.096	0.40	3.1	52.1	18.93/20.92	19.78/19.83	1	quasar+star
J074922.96+225511.7	2.166	0.46	3.8	56.1	19.18/20.78	20.02/21.39	1	dual quasar^a
J075350.57+424743.9	1.523	0.33	2.8	306.9	18.06/21.49	18.93/20.43	1	quasar+star
J075824.26+145752.4	2.568	0.50	4.0	69.0	19.58/21.90/23.57	20.07/21.54/21.93	1	quasar+stars
J081603.79+430521.1	0.586	0.72	4.8	275.3	20.61/22.34	21.75/20.65	4	quasar+star^c
J082341.08+241805.6	1.811	0.64	5.4	183.2	18.19/18.58	18.54/18.86	4	dual/lensed quasar
J084129.77+482548.4	2.949	0.46	3.5	132.0	19.48/19.81	20.04/20.61	1	dual quasar^a
J090408.66+333205.2	1.103	0.30	2.5	104.2	18.65/20.69	19.75/20.08	1	quasar+star
J090501.12+585902.5	2.386	0.61	5.0	228.0	18.62/22.87	19.72/21.36	1	quasar+star
J091826.08+351243.1	1.521	0.18	1.6	260.3	19.13/21.92	19.75/20.10	1	quasar+star
J091938.93+621951.1	1.270	0.69	5.7	333.3	19.11/22.61	19.65/20.39	4	quasar+star
J094007.41+334609.5	1.784	0.74	6.2	239.2	19.81/20.89	20.31/20.07	4	quasar+star
J105929.04−503739.5	0.25 [†]	0.54	2.1	223.2	19.00/22.62	19.45/21.20	3	quasar+star
J122734.48−491202.5	0.25 [†]	0.50	1.9	301.8	20.71/21.28	20.74/20.89	6	quasar+star
J131416.01−491218.2	2.29	0.52	4.2	160.5	19.38/20.93/24.26	20.13/19.65/22.27	6	quasar+stars^b
J161349.51−264432.5	1.1 [†]	0.28	2.3	250.5	20.02/23.19	20.78/21.67	2	quasar+star
J164818.07+415550.1	2.393	0.44	3.5	39.9	18.40/21.02	19.44/21.79	1	dual/lensed quasar
J164941.29+081233.5	1.4 [†]	0.59	5.0	1.9	19.07/19.73	19.55/20.26	5	dual/lensed quasar
J171139.97−161147.9	0.75 [†]	0.67	4.9	128.6	20.69/20.99/24.87	20.34/20.76/22.66	5	dual/lensed quasar+star
J173222.88−133535.2	0.292	0.72	3.2	329.0	19.98/21.37	19.43/21.08	2	quasar+star^b
J175543.18+422924.2	1.95 [†]	0.59	5.0	12.0	17.72/21.85	18.57/20.86	5	quasar+star
J180409.55+323029.5	0.504	0.68	3.6	181.2	19.09/20.68	20.23/20.15	5	quasar+star^b
J184520.85−232227.6	0.8 [†]	0.66	5.0	170.4	19.51/20.04	19.88/20.02	5	dual/lensed quasar
J185226.10+483315.0	1.480	0.62	5.2	190.6	18.94/22.49	19.80/21.65	2	quasar+star^b
J185728.65+704811.3	1.230	0.61	5.0	160.4	19.87/23.15	20.47/20.27	5	quasar+star^b

Table 3 continued

Table 3 (*continued*)

Name	Redshift	$\Delta\theta$	r_p	P.A.	F475W	F814W	Cat.	Classification
		[arcsec]	[kpc]	[deg]	[mag]	[mag]		
(1)	(2)	(3)	(4)	(5)	(6)	(7)	(8)	(9)
J193718.81–182132.2	1.2 [†]	0.62	5.2	188.4	20.25/20.59	21.09/20.98	5	dual/lensed quasar
J194349.74–023819.1	1.6 [†]	0.66	5.6	174.7	19.25/21.04	19.79/20.57	5	quasar+star
J204848.00+625858.3	2.5 [†]	0.62	5.0	297.1	20.33/20.87	20.58/20.94	5	dual/lensed quasar
J205000.01–294721.7	1.75 [†]	0.65	5.5	280.4	19.18/20.64	19.59/20.67	5	dual/lensed quasar
J212243.01–002653.8	1.975	0.52	4.4	313.8	19.20/20.38	19.96/20.48	4	dual/lensed quasar
J215444.04+285635.3	0.723	0.68	4.9	193.0	19.53/20.89	20.90/20.98	4	quasar+star
J221849.86–332243.6	2.0 ^e	21.11/21.25/21.89/22.73	21.10/21.30/21.77/22.68	5	quad lens
J232412.70+791752.3	0.4 [†]	0.49	2.7	310.5	17.58/18.93	17.55/19.57	2	dual/lensed quasar

NOTE—Col. 1: J2000 coordinates in the form of “hhmmss.ss±ddmmss.s”. Col. 2: Spectroscopic redshift or photometric redshift when denoted with “†”. Col. 3: Angular separation. Col. 4: Projected physical separation based on the redshift. Col. 5: Position Angle between the two brightest sources in degree east of north. Col. 6: *HST* F475W ST magnitude of each source. Col. 7: *HST* F814W ST magnitude of each source. Col. 8: Target Category. Col. 9: Best-effort classification. The term “stars” in classification means more than one PSF components with star-like color, instead of an extended source. Targets which are confirmed spectroscopically are marked in bold.

^aSee detailed discussion in Shen et al. (2021).

^bThe classifications are based on the spatially resolved optical spectra from Gemini.

^cThe classification is based on the unresolved SDSS spectra.

^dThe targets reveal irregular merger features.

^eUsing a fiducial redshift of 2.0 for the quadruply lensed quasar. The photo-z is biased due to the contamination of the foreground galaxy

3. RESULTS

2.5. Initial Optical Spectroscopic Follow-up Observations

We are conducting follow-up observations of *HST*-resolved pairs, and will present the final results of our follow-up observations in a future paper. Here we present confirmation and redshift measurements from ground-based Gemini optical spectroscopy for the subset of targets that have been followed-up so far.

The Gemini GMOS spectroscopic follow-ups (GN-2020A-DD-106 and GS-2020A-DD-106; PI: Liu, GN-2020A-Q-232; PI: Chen) were conducted between February 2020 and August 2020 for seven targets. The spectra cover the observed wavelength of 4000Å–10040Å with a resolving power R of 421. We are able to decompose the (marginally) spatially resolved sources and obtain the spectra of each source for six targets, except for J0904+3332 due to its small pair separation of 0".3. Out of the six targets, one is the a dual quasar reported in Shen et al. (2021) and five are star-quasar superpositions, whose spectra are shown in Figure 7.

We present our *HST* follow-up observations of the 84 observed targets. Figure 3 shows the *HST* color-composite images of the 45 targets that have sub-arcsec multiple cores resolved at the *HST* resolution. Figure 4 shows the *HST* images of the remaining 39 targets which have a single unresolved core with *HST*. Among the 45 quasars with multiple cores in *HST*, 26 have multiple *Gaia* source matches and 19 have a single matched source in *Gaia*.

We perform GALFIT decomposition of the *HST*-resolved targets, and compile the decomposed PSF fluxes in Table 3. We classify each target based on the morphology, color information as well as follow-up spectroscopy. For the 39 single *HST*-unresolved sources, the target is classified as “unresolved single” if a single PSF can well fit the surface brightness ($\chi^2_\nu < 1.3$ in the 6"×6" F814W GALFIT region); otherwise the target is classified as “extended host” when additional Sérsic components are needed to reduce χ^2_ν . For the 45 quasars showing multiple sources in *HST*, we use color information of each core to distinguish star-quasar superposition (see §3.1 for details) along with follow-up

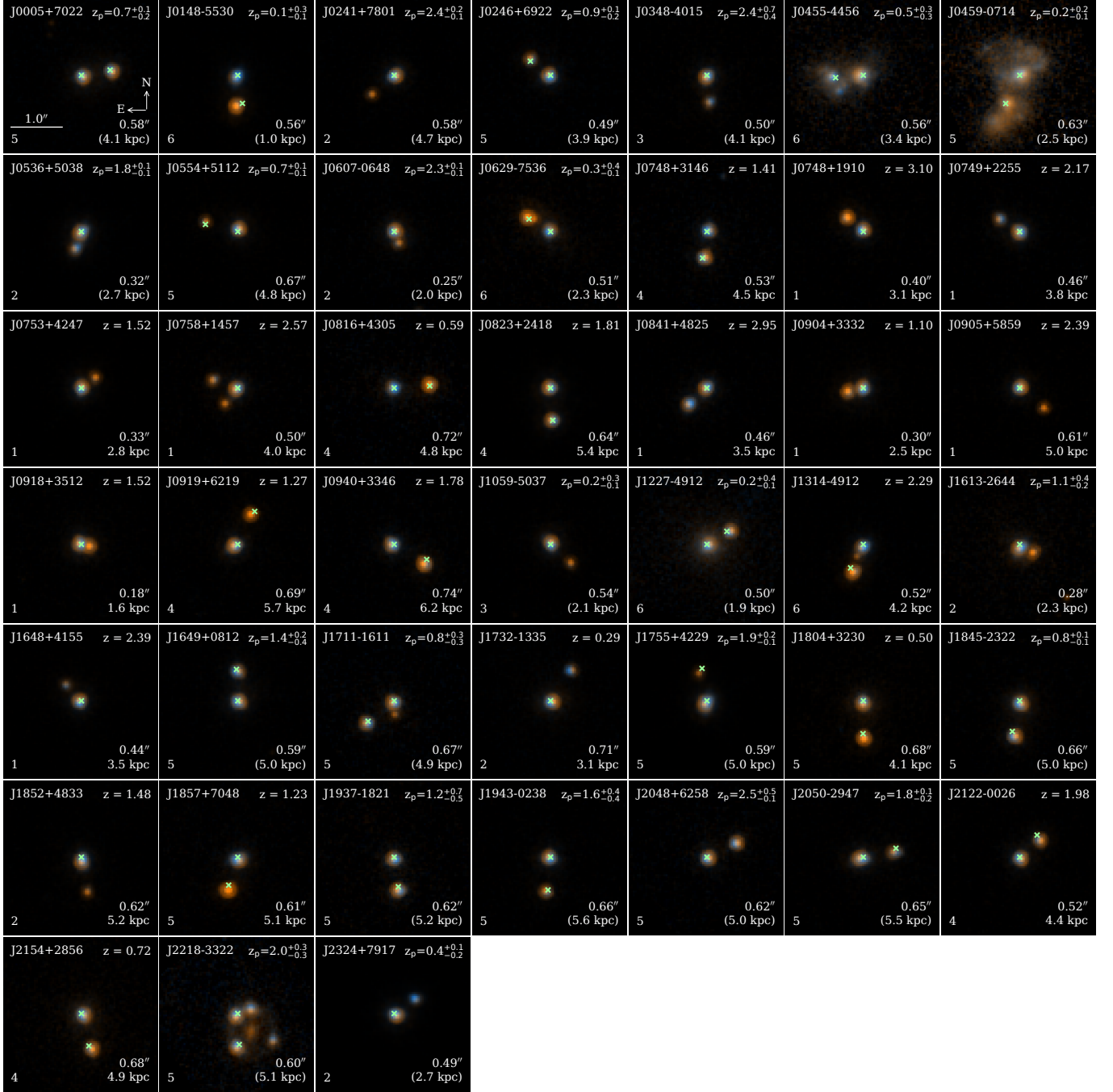


Figure 3. *HST*/WFC3 color composite images (F475W in blue, F814W in red, and the average of F475W and F814W in green) of the 45 targets showing multiple sources in the *HST* images. North is up and east is to the left. The *Gaia* DR2 source positions are marked by the green crosses. Labeled in each panel are the angular and physical separations between the double sources (physical separations calculated using photo-zs are in parentheses). The target category of each source is labeled in the bottom-left corner.

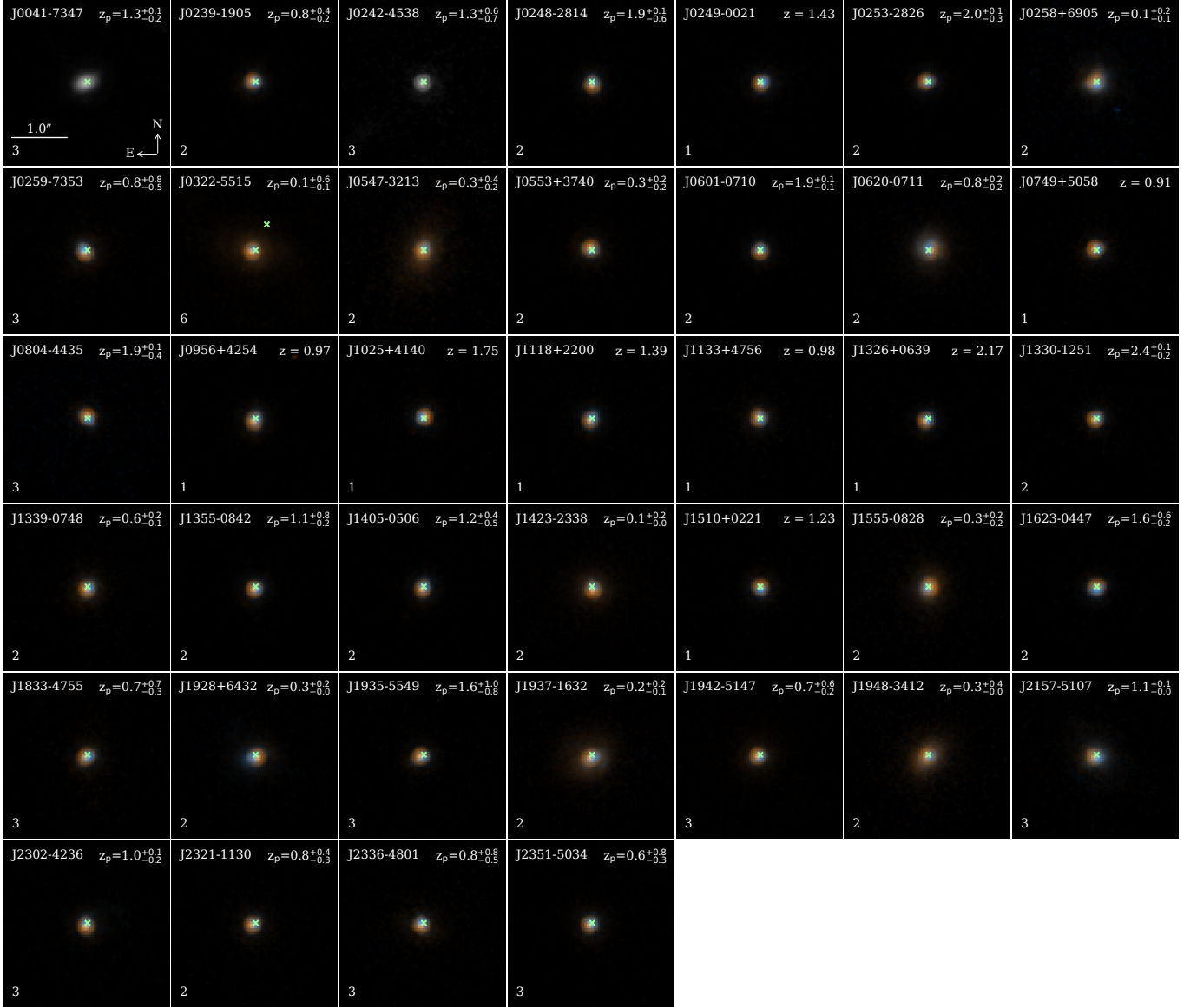


Figure 4. Same as Fig. 3, but for the 39 targets that appear single in *HST* imaging.

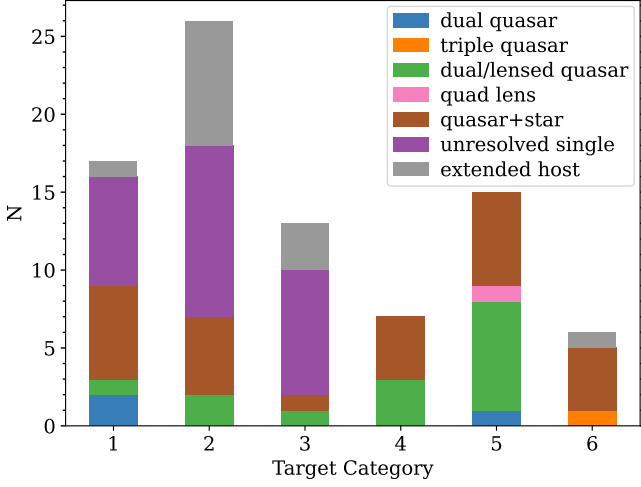


Figure 5. Numbers of targets for each classification in the six target categories. The six target categories are: 1. SDSS Single, 2. WISE+PS1 Single, 3. WISE-only Single, 4. SDSS Multiple, 5. WISE+PS1 Multiple, and 6. WISE-only Multiple. The details of each target category are described in subsection 2.1.

spectroscopy for several targets. If the system has a red color in either core or has a large color difference, it is classified as “quasar+star” and as “dual/lensed quasar” if the colors of both cores are quasar-like.

In addition to the classifications defined above, we also add “dual quasar”, which include the two confirmed dual quasars (J0749+2255 and J0841+4825) from Shen et al. (2021) and a dual quasar candidate (J0459–0714) showing a tidal feature, “triple quasar”, which includes a triple quasar candidate (J0455–4456) showing a tidal feature, and “quad lens”, which includes a quadruply lensed quasar (J2218–3322) with the Einstein ring and the central lens galaxy. The classification for each of those targets is discussed in detail in §3.3.

Our *HST* program has revealed a large fraction of resolved sub-arcsec pairs in our *Gaia*-selected quasar targets; additional follow-up observations are required to confirm the nature of these resolved pairs. We summarize our source classifications for the six target categories in Figure 5. Below we provide our best effort in classifying these resolved pairs based on the existing data.

3.1. Chance Superposition with Stars

The dual-band *HST* colors can be used to assess the likelihood of star-quasar superposition. If the resolved pairs have similar optical colors, they are more likely to be both quasars (either a dual quasar or a lensed quasar). However, there are exceptions where the physical quasar pairs can have different colors such as the $z=1.285$ dual quasar (with a separation of $1''.67$) SDSS J233646.2–010732.6, which consists of a standard

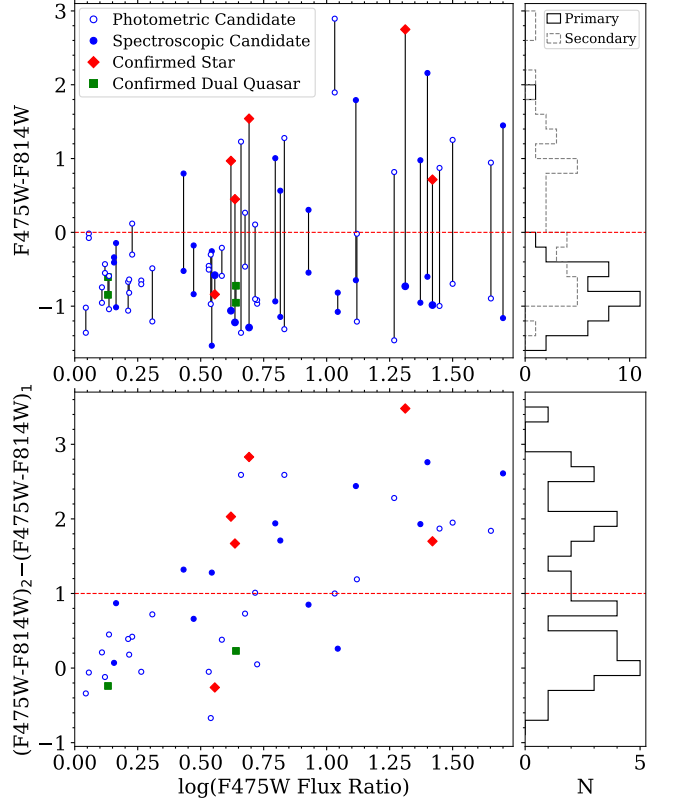


Figure 6. *Top:* $F475W-F814W$ color vs. $F475W$ flux ratio of two sources for the 45 targets with *HST*-resolved multiple sources. The black vertical lines connect two sources in the same system. *Bottom:* $F475W-F814W$ color difference vs. $F475W$ flux ratio of the two sources. For targets with more than two sources, we only plot the two brightest sources. The red diamonds represent the spectroscopically confirmed star-quasar superpositions, the green squares represent the two confirmed dual quasars in Shen et al. (2021), and the filled (open) circles represent the systems with spectroscopic (photometric) redshift. The red dashed lines represent the two color selection criteria for identifying stars.

quasar with a blue continuum and a broad absorption line (BAL) quasar (Gregg et al. 2002).

We use the $F475W-F814W$ color to identify possible star-quasar superpositions. Given some of the targets are at low Galactic latitudes, we correct for the Galactic extinction with DUSTMAPS (Green 2018) using the Schlegel, Finkbeiner & Davis (SFD) map of interstellar dust (Schlegel et al. 1998) and convert the $E(B-V)$ values in SFD to extinctions in the *HST* $F475W$ and $F814W$ filters using Table 6 in Schlafly & Finkbeiner (2011) for $R_V = 3.1$. The de-reddened $F475W-F814W$ colors of each source for the 45 *HST*-resolved pairs are shown in the top panel of Figure 6. The color differences (color of the fainter source minus color of the brighter source) within each pair are presented in the bottom panel of Figure 6.

We use two criteria to identify possible star-quasar superpositions:

1. $F475W - F814W > 0$ mag, OR
2. $(F475W - F814W)_2 - (F475W - F814W)_1 > 1$ mag,

where 1 is the brightest source in $F475W$ and 2 is the second brightest (or faintest) source in $F475W$. The system is classified as a star-quasar pair if it meets either criterion. For the few targets with three sources, we use the $F475W - F814W$ color of each source and the color difference between the brightest source and the second brightest (or faintest) source to identify possible star contamination.

We convolve quasar’s SED templates from [Vanden Berk et al. \(2001\)](#); [Glikman et al. \(2006\)](#) and stellar templates from [Pickles \(1998\)](#) with *HST* bandpasses using PYSYNPHOT to produce the synthetic $F475W - F814W$ colors of canonical quasars and different types of stars. The colors of quasars at $z = 0 - 3$ are between -0.3 and -1.0 mag. The first criterion separates quasars from foreground K and M type stars. Though we cannot separate F and G type stars from quasars due to similar continuum slope, they should be much rarer than K and M type stars ([Kroupa et al. 1993](#); [Kirkpatrick et al. 2012](#); [Bovy 2017](#)). The second criterion removes those with large color discrepancy, which are likely to be star-quasar superpositions. The caveat of the color selections is that it will remove real quasar pairs with different colors such as normal+BAL quasars. It is also noted that some stars might be unresolved compact stellar clusters in a companion galaxy, whose two-band *HST* colors may be similar to those of single stars.

There are five star-quasar superpositions confirmed by Gemini long-slit spectroscopy, shown in [Figure 7](#). The stellar absorption features are seen in the spectra of all the companions. J1857+7048 shows strong metal absorption lines which indicates that the companion is an M type star. The Na I $\lambda\lambda$ 5890, 5896 Å absorption lines as well as the Ca II $\lambda\lambda$ 8498, 8542, 8662 Å lines are seen in J1314+4912, J1804+3230 and J1852+4833, suggesting that their companions are K type stars. Though the interstellar medium in the Milky Way can also produce Na I absorption lines ([Murga et al. 2015](#)), we only see Na I lines in the companion’s spectrum but not in the quasars spectrum, which disfavors this scenario. As for J1732–1335, the narrow H α absorption line at 6563 Å indicates that the companion is a G type star; the weak emission at 8479 Å is the flux leakage from the quasar due to the high flux contrast between the two cores and the marginally resolved spectra. With one additional confirmed case (J0816+4305) from its SDSS unresolved spectrum (missed during our initial *HST* target selec-

tion), six targets have been spectroscopically confirmed as star-quasar superpositions. They are shown as red filled diamonds in [Figure 6](#).

All the spectroscopically confirmed star-quasar superpositions are correctly identified using our color cuts except for J1732–1335, whose companion is likely a G type star. This test suggests our two color criteria are reasonable in identifying star-quasar pairs with an estimated success rate of 80% (i.e., 5/6). Based on these two color criteria and the follow-up spectroscopic observations, we classify 26 of the 45 *HST* multiples as (potential) star-quasar superpositions.

3.2. Star-quasar Superposition Probability

We estimate the probability of star-quasar superposition for the SDSS quasars (Category 1) by considering their surrounding stellar density. We start with the parent quasar sample which the *HST* SDSS targets are selected from ([Hwang et al. 2020](#)). Specifically, for this parent quasar sample, we require that there is only a single *Gaia* match within 3 arcsec with a G-band magnitude < 19.5 , `visibility_periods_used` ≥ 9 , and $z > 0.5$, resulting in a sample of $\sim 79,000$ quasars. Then, we offset their declination by 1 arcminute and search for nearby *Gaia* DR2 sources at the offset positions. All nearby sources around the offset coordinates are considered as star-quasar pairs. Because the star-quasar superposition rate depends on the surrounding stellar density, which further depends on the Galactic coordinates, our test ensures that the offset coordinates have similar Galactic coordinates (differ by only 1 arcmin) and therefore have similar star-quasar superposition rate as the original parent sample.

Our star-quasar superposition test finds that there are 11 offset coordinates that have another fainter source within $0''.5$ (given the mean angular separation of $0''.406$ for the single-*Gaia*-match quasars with *HST* double cores). We only consider the pairs where the nearby sources are fainter than the quasars in *Gaia* G-band because a superposition of a quasar with a brighter stellar object would be removed from our sample by their stellar features in SDSS spectra, or is not included in the SDSS quasar catalog in the first place. Since *Gaia* DR2’s completeness of nearby source identification drops significantly below $0''.7$ ([Arenou et al. 2018](#)), we expect that most of these 11 pairs would remain unresolved in *Gaia* DR2 and appear as single-*Gaia*-match quasars. If these 11 mock pairs all have sufficiently high astrometric excess noise and become our *HST* targets, then the stellar contamination fraction among the 40 single-*Gaia*-matched *HST* targets (i.e., Category 1) is at most $30 \pm 10\%$ (assuming Poisson noise). This is a hard up-

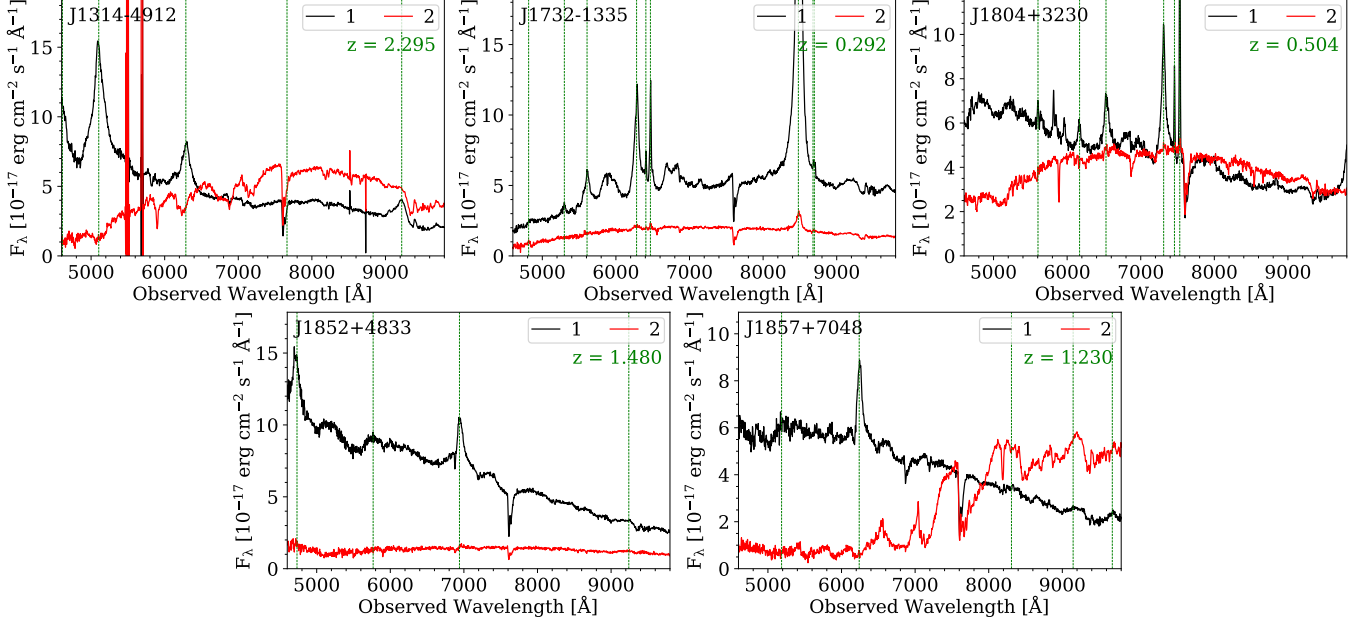


Figure 7. Gemini GMOS optical spectra of the 5 confirmed star-quasar superpositions. Quasar’s spectra are in black and star’s spectra are in red. The green vertical lines mark the quasar’s emission lines at the given redshift shown in the top-right corner.

per limit because some of them can be excluded by the stellar spectral features when the star is not much fainter than the quasar, and more importantly, star-quasar pairs may not necessarily have high astrometric excess noise that fall into our selection. For comparison, our color criteria identify 6 star-quasar pairs out of the 17 observed targets in Category 1, which results in a contamination rate of 6/17 (35%), in broad agreement with this shifted position test.

3.3. Dual Quasars versus Lensed Quasars

The primary goal of our program is to discover \sim kpc-scale dual quasars, especially at $z > 1$. As illustrated in Figure 1, our targeted search has the potential to fill a redshift-separation regime largely uncharted by previous searches for dual quasars. We have followed up some promising candidate high-redshift kpc-scale dual quasars from the resolved 45 systems. J0749+2255 and J0841+4825 have been reported in Shen et al. (2021), and favor the dual quasar scenario (although the lensed quasar scenario cannot be entirely ruled out). Based on statistical arguments, Shen et al. (2021) argued that the abundance of high-redshift sub-arcsec gravitational lens is insufficient to account for most of the resolved pairs in our systematic search.

Besides the spectroscopically confirmed dual quasars and star-quasar superpositions, the *HST* images revealed diagnostic morphology such as tidal features or lens galaxies in several targets (Figure 8). J0455–4456 is classified as a triple quasar candidate, which shows

an irregular tidal feature in the images and the F475W–F814W colors of its three sources are consistent with quasar color. Similar tidal features are seen in J0459–0714, which is likely a dual quasar. On the other hand, a lens galaxy and a weak Einstein ring in J2218–3322 confirm the lensing scenario. J2218–3322 is among the smallest-separation quadruply lensed quasars (Blackburne et al. 2008). Besides J0455–4456, there are also four targets (J0629–7536, J0758+1457, J1314–4912 and 1711–1611) consisting of three components, although not all components are classified as quasars based on their colors in each target. Those four targets are likely a dual/lensed quasar with a star or a quasar with two stars.

For other pairs without distinctive features, the hypothesis of lensed quasars cannot be easily ruled out. Our *HST* optical imaging is too shallow and inefficient to rule in/out high-redshift lens in individual systems, except in rare cases where a potential lens is detected (e.g. J2218–3322) or a merger feature is seen (e.g. J0455–4456 and J0459–0714), supporting the dual quasar classification. Besides, given the general similarity of quasar spectra, nearly identical spectra do not necessarily imply a lensed quasar. For example, SDSS J1124+5710 and SDSS J1309+5617 in More et al. (2016) have nearly identical spectra, but the slight differences in the emission line shapes and redshifts suggest that they are probably physical pairs. Future high-resolution IR imaging and spatially resolved spec-

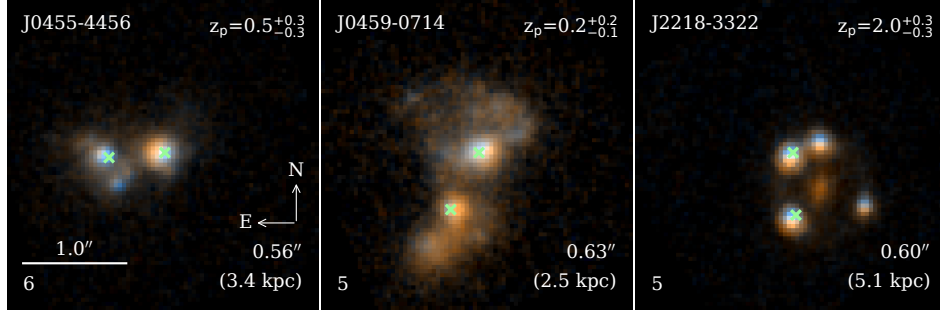


Figure 8. *HST*/WFC3 color composite images of three highlighted targets. *Left:* A triple quasar candidate with irregular tidal feature. *Middle:* A dual quasar candidate with irregular tidal feature. *Right:* A quadruply lensed quasar.

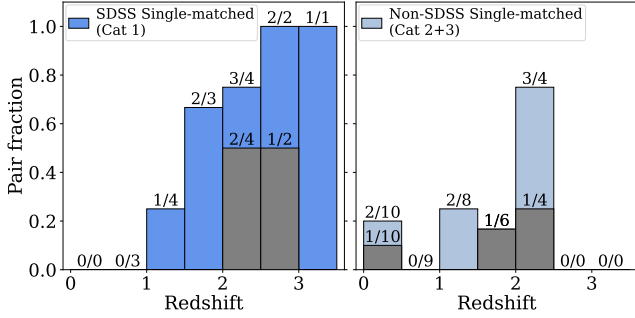


Figure 9. Pair fraction of the *Gaia* single-matched targets (i.e., *varstrometry* selection) as a function of redshift. The pair fraction is defined as the number of doubles/multiples regardless of their physical nature divided by the number of *HST*-observed targets. The values are also denoted on top of each bin. In addition to the pair fraction, the dual/lensed quasar fraction is shown in the grey histogram. *Left:* The SDSS single-matched targets only. *Right:* The non-SDSS single-matched targets. The redshifts are from photo-*z*s if spectroscopic redshifts are unavailable.

troscopy are essential to distinguish dual quasars from lensed quasars.

4. DISCUSSION

4.1. *Varstrometry* Selection Efficiency Increases with Redshift

Among the *Gaia* single-matched targets observed by *HST*, those with spectroscopic redshifts from SDSS (Category 1) have the highest pair fraction of 53% and those from PS1+WISE (Category 2) have a moderate pair fraction of 27%; in contrast, those with WISE-only selection (Category 3) have the lowest pair fraction of 15% (Table 1). The high success rate of the SDSS targets is expected given that we were able to exclude the low-redshift ($z < 0.5$) targets. As for the PS1+WISE targets, without spectroscopic redshifts, the sample might still contain low- z host galaxies that are unresolved in PS1, which slightly reduces the observed pair fraction. The lowest success rate of the WISE-only targets is likely due to the lack of optical imaging in-

formation to exclude the contamination from extended host galaxies or the complicated selection criteria to remove the low- z extended galaxy that might also reject possible doubles.

To better demonstrate the host galaxy contamination at low redshift, we show the pair fraction of the *Gaia* single-matched targets as a function of redshift in Figure 9. The pair fraction is the fraction of doubles/multiples regardless of their physical nature among the observed targets. The targets at low redshift ($z < 1$) are more contaminated by extended host emission and have a low success rate of *HST*-resolved pairs. However, the pair fraction increases dramatically at $z > 1$. The high pair fraction at $z > 1$ suggests that the *varstrometry* technique is highly effective in searching for sub-arcsec quasar pairs at high redshift. While our follow-up observations only produced a small number of confirmed dual quasars, there is evidence (Figure 9) that the *varstrometry* selection is efficient in discovering genuine $z > 1$ double quasars (either physical pairs or lensed quasars).

4.2. Separation predicted from *varstrometry*

We test if the separations predicted from *varstrometry* are consistent with the true separations measured in the *HST* images for the 18 pairs with single *Gaia* detections. Hwang et al. (2020) gives the relation between astrometric jitter, separation and fractional photometric variability if astrometric jitter is solely due to the asynchronous flux variations of both members in an unresolved pair. For an unresolved double quasar, if both quasars have the similar fractional variability, the predicted separation (using Equation 3 in Hwang et al. 2020) is

$$D \sim \frac{\sigma_{\text{astro}}}{\sqrt{\frac{2q^2}{(1+q)^2(1+q^2)} \frac{\sqrt{\langle \Delta f^2 \rangle}}{\bar{f}}}}, \quad (1)$$

where D is the separation, σ_{astro} is the astrometric jitter, q is the flux ratio, $\sqrt{\langle \Delta f^2 \rangle}$ is the total flux variability of the system and \bar{f} is the mean flux of the system. For

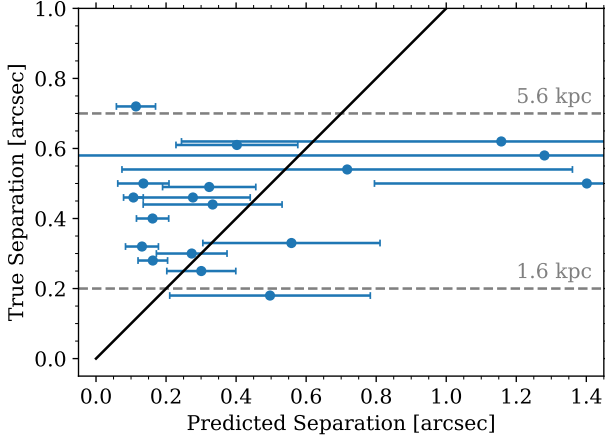


Figure 10. Comparison between the predicted separations from *varstrometry* and the true separations for the 18 pairs with single *Gaia* detections. The black line shows the unity relation. The grey lines are the corresponding physical separations for 0.2 arcsec (1.6 kpc) and 0.7 arcsec (5.6 kpc) at $z = 1$. At these scales, both black holes are within the potential of the merged galaxy and follow orbital decay due to dynamical friction.

an unresolved star-quasar superposition, in which only one member is variable, the predicted separation (using Equation 5 in Hwang et al. 2020) is

$$D \sim \frac{\sigma_{\text{astro}}}{\frac{q}{1+q} \sqrt{\langle \Delta f^2 \rangle}}. \quad (2)$$

The astrometric jitter σ_{astro} is calculated as the root sum of square of *astrometric_excess_noise*, parallax and proper motion in the 22-month observing period of *Gaia* DR2. The flux variability $\sqrt{\langle \Delta f^2 \rangle}$ is estimated as *phot_g_mean_flux_error* times the square root of *phot_g_n_obs*. We subtract the flux variability by the measurement uncertainty (using all sources with similar magnitudes ($\Delta m < 0.1$) within a radius of 0.5 degree) to obtain the quasar-induced intrinsic photometric variability. The flux ratio in *Gaia* *G*-band is estimated from the interpolation of the *HST* dual-band fluxes. We apply Equation 1 to the targets classified as dual/lensed quasars and Equation 2 to those classified as star-quasar superpositions. Figure 10 shows the comparison between the predicted separations from *varstrometry* and the true separations for the 18 pairs with single *Gaia* detections. Two thirds of the targets are within 1- σ uncertainties. The predicted separations are broadly consistent with the true separations, supporting *varstrometry* as the origin of astrometric jitters, although the data points are not tight enough to reject other systematics. We found that targets with separations of $\gtrsim 0''.5$ have larger offsets from the expected values, which is likely because the large pair sep-

aration makes the light profile deviate from a single PSF. In practice, it is difficult to predict the separations precisely based on the approximate *varstrometry* formula. We suspect that the 0.2-0.7 arcsec range is mostly a selection effect. For pairs with separations of $\gtrsim 0.8$ arcsec, *Gaia* would likely already resolve the source; on the other hand, *HST* cannot resolve the pair with separations of $\lesssim 0.2$ arcsec), but the expected shorter dynamical time at smaller separations might play some role here as well.

4.3. *HST*-unresolved Sources

Besides the sub-arcsec doubles/multiples resolved by *HST*, there are 39 *HST* unresolved targets. Several possibilities could explain those unresolved sources: *varstrometry* may be able to detect doubles that are unresolved by *HST*, extended host emission could contribute extra astrometric noise, or they are caused by *Gaia* systematics. 13 ($\sim 33\%$) of the 39 *HST* unresolved sources contain significant extended emission from host galaxies (Figure 5) and are at low redshift ($z \lesssim 1$) based on the SDSS spectra or photo-zs. Most of the systems classified as extended hosts fall in the categories without spectroscopic redshifts (Categories 2 and 3), which is expected because these categories mainly rely on the astrometric excess noise; extended host emission can contribute to this astrometric excess noise (Hwang et al. 2020). As for the systems from SDSS (Category 1), since low-redshift targets ($z < 0.5$) had been removed, the point-like targets could either be small-scale (< 0.1 arcsec) doubles that are unresolved by *HST* or could be caused by *Gaia* systematics.

There are some interesting targets that cannot be modeled by a single PSF or a PSF with Sérsic components. One such case is J0041–7347, which shows an elongated ellipse with a similar color profile across the ellipse. However, Leisy & Dennefeld (1996) have identified J0041–7347 as a carbon-rich planetary nebula based on optical and ultraviolet spectroscopic observations. The other cases are J0620–0711 and J0258+6905, whose central components deviate from the PSF and show faint offset residuals. The targets with the small offset residuals could be double cores with a separation smaller than the *HST* resolution ($< 0''.1$); however the possibility of an imperfect PSF model cannot be excluded.

4.4. Comparison to other methods

There are several other techniques for finding dual quasars at (sub)kpc scales that are unresolved in ground-based observations. One popular method is double-peaked profiles in narrow emission lines in quasar

spectra (Wang et al. 2009; Liu et al. 2010b; Smith et al. 2010). However, most dual quasars found from the double-peaked narrow-line samples (Liu et al. 2010a; Fu et al. 2012; Comerford et al. 2015) are at low redshifts ($z < 0.5$). In addition, in most cases such double-peaked structure is due to the complex kinematics of the narrow-line region such as rotation and outflows (Shen et al. 2011a; Fu et al. 2012; Zakamska & Greene 2014; Müller-Sánchez et al. 2016); the dual quasar fraction among the double-peaked narrow-line sample is usually few percent (Shen et al. 2011a; Fu et al. 2012). Direct imaging with high-resolution radio interferometers (e.g., VLA and VLBA) is also used to confirm the nature of dual quasar candidates at kpc scales (Fu et al. 2015a,b; Shen et al. 2021) or even at pc scales (Rodríguez et al. 2006) although it requires the source to be radio-bright.

By design, the *varstrometry* selection technique only applies to (optically) unobscured broad-line (i.e., type 1) quasars, where the AGN variability is detectable by *Gaia*. It is possible that kpc dual quasars in high-redshift mergers are more likely to be obscured systems, similar to the cases observed in MIR-selected low-redshift dual AGNs (Satyapal et al. 2017; Pfeifle et al. 2019). We will investigate this possibility in future work by comparing our observational results with cosmological hydrodynamic simulations (Blecha et al. 2013, 2018).

Other indirect methods such as the radial velocity shift of the broad emission lines (Eracleous et al. 2012; Shen et al. 2013; Liu et al. 2014; Runnoe et al. 2017; Wang et al. 2017; Guo et al. 2019) and periodicity in the optical light curves (Graham et al. 2015; Charisi et al. 2016; Liu et al. 2019; Chen et al. 2020b; Liao et al. 2021) are sensitive to binary SMBHs at sub-pc scales, where the two SMBHs become gravitationally bound. Both methods require decade-long multi-epoch imaging or spectroscopy. Those candidates are difficult to resolve with radio interferometers even with VLBI; none of them are confirmed by direct imaging so far.

The high pair fraction of $\sim 30\%$ in the single-*Gaia*-matched quasar sample indicates that the *varstrometry* technique is very effective in finding unresolved pairs. Assuming that $\sim 40\%$ of the pairs are dual/lensed quasars, we expect that $\sim 12\%$ of the candidates selected from *varstrometry* are dual/lensed quasars. The fraction is even higher in the spectroscopically confirmed quasar sample (Category 1).

4.5. Refining Targeting and Follow-up Strategy

Building on the results from this pilot *HST* program, we can refine the targeting strategy to search for dual quasars with high-spatial-resolution imag-

ing/spectroscopy, especially with *varstrometry*, to improve the success rate:

1. The new *Gaia* EDR3 (Gaia Collaboration et al. 2021) provides better astrometric measurements overall. The position uncertainties of objects at the faint end decreased by nearly half, for example, from 0.7 mas in DR2 to 0.4 mas in EDR3 at $G = 20$ (Lindegren et al. 2021). In addition, EDR3 resolves more sub-arcsec pairs than DR2, has better treatments of extended sources, and the reliability of the astrometric excess noise parameter is generally improved over DR2. From the same *varstrometry* selection criteria, the 38 *HST*-unresolved targets (excluding J0322–5515) show *astrometric_excess_noise* of 1.66 ± 0.14 mas, and the 18 *HST*-resolved pairs show higher values of 2.50 ± 1.36 mas, a $\sim 5\sigma$ difference. The higher *astrometric_excess_noise* values of the *HST*-resolved pairs support the hypothesis of *varstrometry* technique. For the *HST*-unresolved targets, the *astrometric_excess_noise* values in EDR3 decrease by 40% on average compared with those in DR2. The improvement on the astrometric excess noise would be particularly useful to reduce false positives selected with *varstrometry* (e.g., those appeared unresolved or with extended host emission in *HST* imaging). We also expect less spurious *Gaia* source detections such as those in J0322–5515.
2. Additional IR imaging with *HST* (or ground-based adaptive optics) is needed to confirm/reject the lensing scenario. The current *HST* F814W optical imaging data are too shallow to detect the lens galaxies, especially for the high- z systems (Shen et al. 2021). Even with spatially-resolved spectroscopy, it is often difficult to rule out the lensing scenario (Shen et al. 2021). High-resolution IR imaging, even at the *HST* SNAP depth, is highly efficient to rule out the lensing scenario by the non-detection of lens galaxies.
3. High-resolution radio imaging could be used to reject star-quasar superposition. Detecting two flat-spectrum compact radio cores will confirm the candidate as a dual/lensed quasar. In addition, if two radio cores have significantly different spectral indices, it will suggest that the source is a dual quasar instead of a lensed quasar. Shen et al. (2021) reported preliminary VLBA observations of J0749+2255, supporting the dual quasar scenario. A few of our targets have detections in publicly available radio surveys such as FIRST (Becker

et al. 1995), NVSS (Condon et al. 1998), and/or VLASS (Lacy et al. 2020), but the angular resolutions of those public radio data are not high enough to resolve the sub-arcsecond pairs.

4. It is more efficient to target spectroscopically confirmed quasars at $z > 1$ than photometric quasar candidates, given the redshift information and potential identification of star-quasar superposition in the spectrum. Indeed, the SDSS **varstrometry**-selected candidates show a high pair detection rate (53%), while the WISE-only candidates only have a pair fraction of 15%, which suggests that the redshift information is crucial to mitigate host galaxy contamination in the astrometric measurements.
5. Wide-field multi-band imaging surveys such as the Dark Energy Survey (Abbott et al. 2018) and DECaLS (Dey et al. 2019) can provide extra morphology and color information. Because of the excellent image qualities (median r -band FWHM of $1''.18$ in DECaLS and $0''.96$ in DES), some pairs with wider separations are marginally resolved and identified. The multi-band colors could also help remove star-quasar superpositions. Among the 14 quasar+star pairs that are covered by DECaLS and DES, we find 8 of them have been identified as two sources, whose separations are $\gtrsim 0''.6$. For the rest 4 quasar+star pairs, 2 of them also show significant red emissions in the residual map.

5. CONCLUSIONS

In this paper, we present *HST* dual-band (F475W and F814W) optical imaging for 56 *Gaia*-unresolved dual quasar candidates selected by **varstrometry** and 28 *Gaia*-resolved dual quasar candidates. These dual quasar candidates are in the sub-arcsec regime, and represent the long-sought kpc-scale dual quasar population.

Our *HST* imaging of the 84 targets reveals 45 resolved pairs (or multiples), among which 17 resolved pairs are from the **varstrometry** selection. The fraction of resolved pairs among the **varstrometry**-selected targets is $\sim 30\text{--}50\%$, increasing toward high redshift ($\sim 60\text{--}80\%$ at $z > 1.5$), with the highest success rate ($\gtrsim 80\%$) in spectroscopically confirmed quasar targets.

We discuss the nature of the 45 *HST*-resolved quasar targets based on *HST* and supplementary data. Given that star-quasar superpositions are a significant contaminant for our sample, we develop color criteria that can successfully reject most of them ($\sim 80\%$). A substantial fraction ($19/45 \sim 40\%$) of the *HST*-resolved pairs are likely physical quasar pairs or gravitationally lensed quasars. It is more probable that most of them are dual

quasars instead of lenses, which require very massive lenses at high redshifts given the non-detection of the lens galaxy in the *HST* image. These systems fill in an important redshift–separation regime of dual SMBHs that has been poorly explored in earlier searches (Figure 1). Besides the candidates selected by colors, we also discover a quadruply lensed quasar, which shows a foreground lens in the *HST* images.

This program with *HST* optical imaging demonstrates the potential of using **varstrometry** and *Gaia* data to systematically discover genuine \sim kpc-scale dual quasars, especially at $z > 1$. Our results provide important guidelines to significantly refine the targeting and follow-up strategy and to facilitate the classifications (§4.5), with improved astrometric measurements from *Gaia* EDR3 and future data releases.

Facilities: *Gaia*, *HST* (WFC3), Gemini (GMOS)

Software: dustmaps (Green 2018), astropy (Astropy Collaboration et al. 2018), pysynphot (STScI Development Team 2013)

We thank J. Blakeslee for granting us Gemini DDT, and K. Chiboucas, H. Kim, and A. Nitta for their help with conducting the Gemini observations, and the referee for useful comments that improved the manuscript. This work is supported by the Heising-Simons Foundation and Research Corporation for Science Advancement, and NSF grant AST-2108162 (YCC, YS, XL). YCC and XL acknowledge support from the University of Illinois Campus Research Board. YCC acknowledges support by the government scholarship to study abroad from the ministry of education of Taiwan and support by the Illinois Survey Science Graduate Student Fellowship. YS acknowledges partial support from NSF grant AST-2009947. NLZ and HCH acknowledge support by the HST-SNAP-15900 grant administered by the STScI.

Based on observations made with the NASA/ESA Hubble Space Telescope, obtained at the Space Telescope Science Institute, which is operated by the Association of Universities for Research in Astronomy, Inc., under NASA contract NAS 5-26555. These observations are associated with program number SNAP-15900.

Based on observations obtained at the international Gemini Observatory (Program IDs GN-2020A-DD-106, GS-2020A-DD-106, and GN-2020A-Q-232), a program of NSF's NOIRLab, which is managed by the Association of Universities for Research in Astronomy (AURA) under a cooperative agreement with the National Science Foundation. on behalf of the Gemini Observatory partnership: the National Science Foundation (United States), National Research Council (Canada), Agencia

Nacional de Investigación y Desarrollo (Chile), Ministerio de Ciencia, Tecnología e Innovación (Argentina), Ministério da Ciência, Tecnologia, Inovações e Comunicações (Brazil), and Korea Astronomy and Space Science Institute (Republic of Korea). This work was en-

abled by observations made from the Gemini North telescope, located within the Maunakea Science Reserve and adjacent to the summit of Maunakea. We are grateful for the privilege of observing the Universe from a place that is unique in both its astronomical quality and its cultural significance.

REFERENCES

- Abbott, T. M. C., Abdalla, F. B., Allam, S., et al. 2018, *ApJS*, 239, 18
- Anguita, T., Schechter, P. L., Kuropatkin, N., et al. 2018, *MNRAS*, 480, 5017
- Arenou, F., Luri, X., Babusiaux, C., et al. 2018, *A&A*, 616, A17
- Arzoumanian, Z., Baker, P. T., Brazier, A., et al. 2018, *ApJ*, 859, 47
- Astropy Collaboration, Price-Whelan, A. M., Sipőcz, B. M., et al. 2018, *AJ*, 156, 123
- Becker, R. H., White, R. L., & Helfand, D. J. 1995, *ApJ*, 450, 559
- Begelman, M. C., Blandford, R. D., & Rees, M. J. 1980, *Nature*, 287, 307
- Bianchi, S., Chiaberge, M., Piconcelli, E., Guainazzi, M., & Matt, G. 2008, *MNRAS*, 386, 105
- Blackburne, J. A., Wisotzki, L., & Schechter, P. L. 2008, *AJ*, 135, 374
- Blecha, L., Loeb, A., & Narayan, R. 2013, *MNRAS*, 429, 2594
- Blecha, L., Snyder, G. F., Satyapal, S., & Ellison, S. L. 2018, *MNRAS*, 478, 3056
- Bogdanovic, T., Miller, M. C., & Blecha, L. 2021, *Living Reviews in Relativity*, arXiv:2109.03262
- Bothun, G. D., Halpern, J. P., Lonsdale, C. J., Impey, C., & Schmitz, M. 1989, *ApJS*, 70, 271
- Bovy, J. 2017, *MNRAS*, 470, 1360
- Brotherton, M. S., Gregg, M. D., Becker, R. H., et al. 1999, *ApJL*, 514, L61
- Burke-Spolaor, S. 2011, *MNRAS*, 410, 2113
- Centrella, J., Baker, J. G., Kelly, B. J., & van Meter, J. R. 2010, *Reviews of Modern Physics*, 82, 3069
- Chambers, K. C., Magnier, E. A., Metcalfe, N., et al. 2016, *arXiv e-prints*, arXiv:1612.05560
- Charisi, M., Bartos, I., Haiman, Z., et al. 2016, *MNRAS*, 463, 2145
- Chen, Y., Yu, Q., & Lu, Y. 2020a, *ApJ*, 897, 86
- Chen, Y.-C., Liu, X., Liao, W.-T., et al. 2020b, *MNRAS*, 499, 2245
- Civano, F., Elvis, M., Lanzuisi, G., et al. 2010, *ApJ*, 717, 209
- Comerford, J. M., Pooley, D., Barrows, R. S., et al. 2015, *ApJ*, 806, 219
- Comerford, J. M., Pooley, D., Gerke, B. F., & Madejski, G. M. 2011, *ApJL*, 737, L19
- Condon, J. J., Cotton, W. D., Greisen, E. W., et al. 1998, *AJ*, 115, 1693
- Crampton, D., Cowley, A. P., Hickson, P., et al. 1988, *ApJ*, 330, 184
- Crotts, A. P. S., Bechtold, J., Fang, Y., & Duncan, R. C. 1994, *ApJL*, 437, L79
- De Rosa, A., Vignali, C., Bogdanović, T., et al. 2020, *arXiv e-prints*, arXiv:2001.06293
- Dey, A., Schlegel, D. J., Lang, D., et al. 2019, *AJ*, 157, 168
- Eftekharzadeh, S., Myers, A. D., Hennawi, J. F., et al. 2017, *MNRAS*, 468, 77
- Ellison, S. L., Secrest, N. J., Mendel, J. T., Satyapal, S., & Simard, L. 2017, *MNRAS*, 470, L49
- Eracleous, M., Boroson, T. A., Halpern, J. P., & Liu, J. 2012, *ApJS*, 201, 23
- Foord, A., Gültekin, K., Runnoe, J. C., & Koss, M. J. 2021, *ApJ*, 907, 71
- Frey, S., Paragi, Z., An, T., & Gabányi, K. É. 2012, *MNRAS*, 425, 1185
- Fu, H., Myers, A. D., Djorgovski, S. G., et al. 2015a, *ApJ*, 799, 72
- Fu, H., Wrobel, J. M., Myers, A. D., Djorgovski, S. G., & Yan, L. 2015b, *ApJL*, 815, L6
- Fu, H., Yan, L., Myers, A. D., et al. 2012, *ApJ*, 745, 67
- Fu, H., Zhang, Z.-Y., Assef, R. J., et al. 2011, *ApJL*, 740, L44
- Gaia Collaboration, Brown, A. G. A., Vallenari, A., et al. 2018, *A&A*, 616, A1
- . 2021, *A&A*, 649, A1
- Glikman, E., Helfand, D. J., & White, R. L. 2006, *ApJ*, 640, 579
- Goulding, A. D., Pardo, K., Greene, J. E., et al. 2019, *ApJL*, 879, L21
- Graham, M. J., Djorgovski, S. G., Stern, D., et al. 2015, *MNRAS*, 453, 1562
- Green, G. 2018, *The Journal of Open Source Software*, 3, 695

- Green, P. J., Myers, A. D., Barkhouse, W. A., et al. 2011, *ApJ*, 743, 81
- Gregg, M. D., Becker, R. H., White, R. L., et al. 2002, *ApJL*, 573, L85
- Guo, H., Liu, X., Shen, Y., et al. 2019, *MNRAS*, 482, 3288
- Hagen, H. J., Hopp, U., Engels, D., & Reimers, D. 1996, *A&A*, 308, L25
- Hennawi, J. F., Strauss, M. A., Oguri, M., et al. 2006, *AJ*, 131, 1
- Hennawi, J. F., Myers, A. D., Shen, Y., et al. 2010, *ApJ*, 719, 1672
- Hewett, P. C., Foltz, C. B., Harding, M. E., & Lewis, G. F. 1998, *AJ*, 115, 383
- Hopkins, P. F., Hernquist, L., Cox, T. J., & Kereš, D. 2008, *ApJS*, 175, 356
- Huang, Y., Liu, X. W., Yuan, H. B., et al. 2014, *MNRAS*, 439, 2927
- Hudson, D. S., Reiprich, T. H., Clarke, T. E., & Sarazin, C. L. 2006, *A&A*, 453, 433
- Hughes, S. A. 2009, *ARA&A*, 47, 107
- Hwang, H.-C., Shen, Y., Zakamska, N., & Liu, X. 2020, *ApJ*, 888, 73
- Inada, N., Oguri, M., Becker, R. H., et al. 2008, *AJ*, 135, 496
- Inada, N., Oguri, M., Shin, M.-S., et al. 2012, *AJ*, 143, 119
- Junkkarinen, V., Shields, G. A., Beaver, E. A., et al. 2001, *ApJL*, 549, L155
- Kharb, P., Lal, D. V., & Merritt, D. 2017, *Nature Astronomy*, 1, 727
- Kirkpatrick, J. D., Gelino, C. R., Cushing, M. C., et al. 2012, *ApJ*, 753, 156
- Komossa, S., Burwitz, V., Hasinger, G., et al. 2003, *ApJL*, 582, L15
- Kormendy, J., & Ho, L. C. 2013, *ARA&A*, 51, 511
- Kormendy, J., & Richstone, D. 1995, *ARA&A*, 33, 581
- Koss, M., Mushotzky, R., Treister, E., et al. 2012, *ApJL*, 746, L22
- . 2011, *ApJL*, 735, L42
- Kroupa, P., Tout, C. A., & Gilmore, G. 1993, *MNRAS*, 262, 545
- Lacy, M., Baum, S. A., Chandler, C. J., et al. 2020, *PASP*, 132, 035001
- Leisy, P., & Dennefeld, M. 1996, *A&AS*, 116, 95
- Lemon, C., Auger, M. W., McMahon, R., et al. 2020, *MNRAS*, 494, 3491
- Lemon, C. A., Auger, M. W., & McMahon, R. G. 2019, *MNRAS*, 483, 4242
- Lemon, C. A., Auger, M. W., McMahon, R. G., & Ostrovski, F. 2018, *MNRAS*, 479, 5060
- Liao, W.-T., Chen, Y.-C., Liu, X., et al. 2021, *MNRAS*, 500, 4025
- Lindgren, L., Lammers, U., Hobbs, D., et al. 2012, *A&A*, 538, A78
- Lindgren, L., Hernández, J., Bombrun, A., et al. 2018, *A&A*, 616, A2
- Lindgren, L., Klioner, S. A., Hernández, J., et al. 2021, *A&A*, 649, A2
- Liu, T., Gezari, S., Ayers, M., et al. 2019, *ApJ*, 884, 36
- Liu, X., Civano, F., Shen, Y., et al. 2013, *ApJ*, 762, 110
- Liu, X., Greene, J. E., Shen, Y., & Strauss, M. A. 2010a, *ApJL*, 715, L30
- Liu, X., Shen, Y., Bian, F., Loeb, A., & Tremaine, S. 2014, *ApJ*, 789, 140
- Liu, X., Shen, Y., Strauss, M. A., & Greene, J. E. 2010b, *ApJ*, 708, 427
- Liu, X., Shen, Y., Strauss, M. A., & Hao, L. 2011, *ApJ*, 737, 101
- Liu, Y. 2015, *A&A*, 580, A133
- Madau, P., & Dickinson, M. 2014, *ARA&A*, 52, 415
- Marrese, P. M., Marinoni, S., Fabrizio, M., & Altavilla, G. 2019, *A&A*, 621, A144
- Mateos, S., Alonso-Herrero, A., Carrera, F. J., et al. 2012, *MNRAS*, 426, 3271
- Mazzarella, J. M., Iwasawa, K., Vavilkin, T., et al. 2012, *AJ*, 144, 125
- McGurk, R. C., Max, C. E., Rosario, D. J., et al. 2011, *ApJL*, 738, L2
- Merritt, D. 2013, *Dynamics and Evolution of Galactic Nuclei*
- More, A., Oguri, M., Kayo, I., et al. 2016, *MNRAS*, 456, 1595
- Morgan, N. D., Burley, G., Costa, E., et al. 2000, *AJ*, 119, 1083
- Müller-Sánchez, F., Comerford, J. M., Nevin, R., et al. 2015, *ApJ*, 813, 103
- Müller-Sánchez, F., Comerford, J. M., Stern, D., & Harrison, F. A. 2016, *ArXiv e-prints* 1606.07446, [arXiv:1606.07446](https://arxiv.org/abs/1606.07446)
- Murga, M., Zhu, G., Ménard, B., & Lan, T.-W. 2015, *MNRAS*, 452, 511
- Murgia, M., Parma, P., de Ruiter, H. R., et al. 2001, *A&A*, 380, 102
- Owen, F. N., O’Dea, C. P., Inoue, M., & Eilek, J. A. 1985, *ApJ*, 294, L85
- Pâris, I., Petitjean, P., Aubourg, É., et al. 2018, *A&A*, 613, A51
- Peng, C. Y., Ho, L. C., Impey, C. D., & Rix, H.-W. 2010, *AJ*, 139, 2097

- Pfeifle, R. W., Satyapal, S., Secrest, N. J., et al. 2019, *ApJ*, 875, 117
- Pickles, A. J. 1998, *PASP*, 110, 863
- Pindor, B., Eisenstein, D. J., Gregg, M. D., et al. 2006, *AJ*, 131, 41
- Richards, G. T., Strauss, M. A., Fan, X., et al. 2006, *AJ*, 131, 2766
- Riello, M., De Angeli, F., Evans, D. W., et al. 2018, *A&A*, 616, A3
- Rodriguez, C., Taylor, G. B., Zavala, R. T., et al. 2006, *ApJ*, 646, 49
- Runnoe, J. C., Eracleous, M., Pennell, A., et al. 2017, *MNRAS*, 468, 1683
- Satyapal, S., Secrest, N. J., Ricci, C., et al. 2017, *ApJ*, 848, 126
- Schechter, P. L., Morgan, N. D., Chehade, B., et al. 2017, *AJ*, 153, 219
- Schlafly, E. F., & Finkbeiner, D. P. 2011, *ApJ*, 737, 103
- Schlegel, D. J., Finkbeiner, D. P., & Davis, M. 1998, *ApJ*, 500, 525
- Secrest, N. J., Dudik, R. P., Dorland, B. N., et al. 2015, *ApJS*, 221, 12
- Shen, Y., Hwang, H.-C., Zakamska, N., & Liu, X. 2019, *ApJL*, 885, L4
- Shen, Y., Liu, X., Greene, J. E., & Strauss, M. A. 2011a, *ApJ*, 735, 48
- Shen, Y., Liu, X., Loeb, A., & Tremaine, S. 2013, *ApJ*, 775, 49
- Shen, Y., Richards, G. T., Strauss, M. A., et al. 2011b, *ApJS*, 194, 45
- Shen, Y., Chen, Y.-C., Hwang, H.-C., et al. 2021, *Nature Astronomy*, 5, 569
- Shields, G. A., Rosario, D. J., Junkkarinen, V., et al. 2012, *ApJ*, 744, 151
- Silverman, J. D., Tang, S., Lee, K.-G., et al. 2020, *arXiv e-prints*, arXiv:2007.05581
- Smith, K. L., Shields, G. A., Bonning, E. W., et al. 2010, *ApJ*, 716, 866
- Springer, O. M., & Ofek, E. O. 2021, *arXiv e-prints*, arXiv:2101.11024
- STScI Development Team. 2013, *pysynphot: Synthetic photometry software package*, , ascl:1303.023
- Tang, S., Silverman, J. D., Ding, X., et al. 2021, *arXiv e-prints*, arXiv:2105.10163
- Teng, S. H., Schawinski, K., Urry, C. M., et al. 2012, *ApJ*, 753, 165
- Vanden Berk, D. E., Richards, G. T., Bauer, A., et al. 2001, *AJ*, 122, 549
- Wang, J., Chen, Y., Hu, C., et al. 2009, *ApJL*, 705, L76
- Wang, L., Greene, J. E., Ju, W., et al. 2017, *ApJ*, 834, 129
- Williams, L. L. R., & Saha, P. 1995, *AJ*, 110, 1471
- Woo, J.-H., Cho, H., Husemann, B., et al. 2014, *MNRAS*, 437, 32
- Wright, E. L., Eisenhardt, P. R. M., Mainzer, A. K., et al. 2010, *AJ*, 140, 1868
- Yang, Q., Wu, X.-B., Fan, X., et al. 2017, *AJ*, 154, 269
- Yu, Q. 2002, *MNRAS*, 331, 935
- Zakamska, N. L., & Greene, J. E. 2014, *MNRAS*, 442, 784